Multi-Omic Analysis Reveals Cannabidiol Disruption of Cholesterol Homeostasis in Human Cell Lines

Steven E. Guard[1,5], Douglas A. Chapnick[2,5], Zachary Poss[1], Christopher C. Ebmeier[1], Jeremy Jacobsen[1], Travis Nemkov[3], Kerri A. Ball[1], Kristofor J. Webb[1], Helen L. Simpson[1] Stephen Coleman[1], Eric Bunker[2], Adrian Ramirez[2], Julie A. Reisz[3], Robert Sievers[4], Michael H.B. Stowell[1], Angelo D'Alessandro[3], Xuedong Liu[2], William M. Old[1,6,*]

[1] Dept. of Molecular, Cellular & Developmental Biology, University of Colorado Boulder
[2] Dept. of Biochemistry, University of Colorado Boulder
[3] Dept. of Biochemistry and Molecular Genetics, University of Colorado Denver
[4] Dept. of Chemistry and Cooperative Institute for Research in Environmental Sciences, University of Colorado Boulder
[5] These authors contributed equally
[6] Lead Contact

*Corresponding Author

Correspondence: william.old@colorado.edu

Summary

Cannabidiol (CBD) is FDA-approved for treatment of drug-intractable forms of pediatric epilepsy, yet the mechanisms that underlie its efficacy remain unclear. Myriad protein targets of CBD have been reported, suggesting a pleiotropic pharmacology. Here, we report a systems-level analysis of CBD action in human cell lines using temporally-resolved multi-omic profiling and biosensor screening. CDB treatment resulted in a chronic rise in cytosolic calcium and activated AMPK signaling within two hours. Subcellular profiling of proteins, metabolites, and mRNA transcripts identified CBD-dependent activation of cholesterol biosynthesis, transport and storage. We found that CBD incorporates into cellular membranes, alters cholesterol chemical activity, and increases lipid order. CBD-induced apoptosis in multiple human cell lines was rescued by inhibition of cholesterol synthesis, and potentiated by compounds that disrupt cholesterol trafficking and storage. Our data point to pharmacological interaction of CBD with cholesterol homeostasis pathways, with potential implications in its therapeutic use.

Keywords: cannabidiol, CBD, systems pharmacology, drug discovery, cholesterol, proteomics, transcriptomics, lipidomics, metabolomics, phosphoproteomics, FRET biosensor, high-content screening, multi-omics

Introduction

The non-psychoactive cannabinoid, cannabidiol (CBD), was recently approved by the FDA for treatment of two drug-resistant epileptic disorders, Lennox-Gastaut syndrome and Dravet syndrome (Devinsky et al., 2017; Miller et al., 2020; Thiele et al., 2018). CBD has an encouraging safety profile across multiple human clinical trials, which has

fueled increased interest in CBD as a therapeutic in other disorders (Iffland and Grotenhermen, 2017). CBD has shown promise as a potential therapeutic from animal model studies of a diverse array of conditions, including oxidative stress and inflammation, chemotherapy associated nephrotoxicity (Pan et al., 2009), colitis (De Filippis et al., 2011), cancer (Hinz and Ramer, 2019; Kenyon et al., 2018; Massi et al., 2013; McAllister et al., 2015), neuroinflammation (Esposito et al., 2011), cardiomyopathy, and diabetic complications (Rajesh et al., 2010). However, CBD treatment has shown an increased risk for liver injury, particularly for patients taking valproic acid (Thiele et al., 2018). Remarkably, despite its promise as a broad therapeutic, the molecular mechanisms that underlie the efficacy and the potential toxicities of CBD in humans remain poorly understood.

CBD has weak affinity (> 3-10 μM) for the endocannabinoid receptor CB_1, and is thus devoid of the psychotropic effects associated with its better known structural isomer, tetrahydrocannabinol (THC) (McPartland et al., 2015). More than 65 protein targets of CBD have been proposed, 22 of which are membrane-localized channels and receptors (Ahrens et al., 2009; Ibeas Bih et al., 2015; Lauckner et al., 2008; Whyte et al., 2009). Notably, CBD inhibits voltage-dependent sodium currents mediated by the NaV1.1 sodium channel (Ghovanloo et al., 2018), mutations in which elicit epilepsy syndromes, including Dravet syndrome (Dravet, 2011). CBD was also shown to inhibit voltage-dependent ion currents of six other human sodium channels, the Kv2.1 potassium channel, and even a bacterial sodium channel, with IC_{50} values 1-3 μM (Ghovanloo et al., 2018). Many proposed targets are calcium channels or receptors that regulate calcium, including T-type calcium channels (Ross et al., 2008), voltage-dependent anion channel 1 (VDAC1) (Rimmerman et al., 2013), G protein-coupled receptor 55 (GPR55) (Lauckner et al., 2008), a voltage-gated calcium channel Cav3.x (Ross et al., 2008), and transient receptor potential cation channels 1-4 (TRPV1-4) (Ibeas Bih et al., 2015). Postsynaptic calcium mobilization has been proposed as a mechanism to explain the anticonvulsant activity of CBD (Gray and Whalley, 2020). The ability of CBD to modulate many structurally diverse membrane channels and receptors has motivated suggestions that CBD, in a similar manner to other amphiphilic molecules such as capsaicin, may act indirectly on membrane proteins through alteration of the biophysical properties of the lipid bilayer (Ghovanloo et al., 2018; Lundbaek et al., 2005; Lundbæk et al., 1996; Watkins, 2019).

Comparatively less is known about intracellular targets and pathways that potentially mediate CBD action in human cells. In microglial cells, CBD has anti-inflammatory activity, and upregulates mRNA transcripts involved in fatty acid metabolism and cholesterol biosynthesis (Rimmerman et al., 2011). In adipocytes, CBD leads to accumulation of triglyceride species, concomitant with phosphorylation changes of upstream lipid metabolism enzymes, and functionally unrelated proteins including CREB, AMPKA2 and HSP60 (Silvestri et al., 2015). In mice, CBD attenuates the liver steatosis and metabolic dysregulation associated with chronic alcohol feeding, further implicating lipid-associated metabolic changes induced by CBD (Wang et al., 2017). The perturbation of transcripts, proteins and metabolites in these studies demonstrates the pleiotropic effects of CBD on diverse molecular classes, and highlights the need for systems-based approaches for examining its mode of action.

Recent advances in mass spectrometry-based omics has enabled nearly comprehensive identification and quantification of cellular proteomes and metabolomes (Blum et al., 2018). Multi-omic profiling strategies that combine mass spectrometry based proteomics with next generation sequencing-based transcriptomics can reveal critical and unexpected insights into the mechanisms of drug action in human cell lines (Hafner et al., 2019; Norris et al., 2017). In this study, we used multi-omic profiling, in combination with FRET-based biosensor microscopy screening, to examine the mode of CBD action in human neuroblastoma and keratinocyte cells. CDB treatment activated 5'-AMP-activated protein kinase (AMPK) and cytosolic calcium signaling within three hours in multiple cell types. In SK-N-BE(2) neuroblastoma cells, proteomics, transcriptomics and lipidomics revealed a concerted upregulation of transcripts and proteins involved in cholesterol import and biosynthesis. We show that CBD sensitized human cells to drugs that interfere with cholesterol trafficking and storage, including an inhibitor of Niemann-Pick C1 (NPC1), U18666A. Using model membranes, we found that CBD increased the chemical activity of cholesterol as a substrate for cholesterol oxidase, while also reducing the lateral diffusion of cholesterol. Our data reveal that a dominant action of CBD involves partitioning into cellular membranes, which leads to the disruption of cholesterol homeostasis. This observation likely underlies the downstream effects of increased apoptosis and the widely reported pharmacological pleiotropy of CBD.

Results

FRET-based sensor array reveals CBD response dynamics

To identify time-ordered molecular events initiated by CBD, we performed temporal multi-omic profiling of CBD treated human neuroblastoma cells, using proteomics, phosphoproteomics, RNA-sequencing (RNAseq) and metabolomics. The dynamics of metabolite, RNA, and protein changes in response to drug perturbation could span time scales ranging from seconds to days, presenting a challenge for selecting appropriate time points in multi-omic analysis. To identify the optimal time points and CBD dose, we monitored a panel of Förster resonance energy transfer (FRET) sensors over time with high-content imaging in human SK-N-BE(2) neuroblastoma cells and HaCaT human keratinocyte cells**.** Transgenic lines were generated, each expressing a genetically encoded FRET biosensor gene capable of reporting the activity of a cellular activity (Chapnick et al., 2019). Sensors were selected to profile a broad range of molecular activities measuring abundances changes in metabolites, secondary messengers as well as kinase and protease activities **(Table S1A).**

FRET ratios were measured in a time course following either vehicle or CBD across a range of doses from 0 to 100 µM **(Figure S1A)**. At each time point, we fit a log-logistic function with the FRET sensor data to estimate EC_{50} values and quantify the dose-dependency for each sensor over time. We found that cytosolic calcium, plasma membrane charge, AMPK activity, ERK activity, and glucose abundance exhibited the most significant dose-dependent changes. A number of sensors showed time dependent responses at various doses of CBD, but showed poor dose-dependency (R^2 <= 0.75), and thus were not used for dose and time range analysis. The EC_{50} distribution of CBD dose across all time points and biosensors displayed a median of

8.5 µM for SK-N-BE(2) cells. We found, however, that 20 µM CBD was required for activation of FRET sensors for which a EC_{50} could be calculated at early time points, including cytosolic calcium, AMPK, and plasma membrane charge **(Figure 1A).** SK-N-

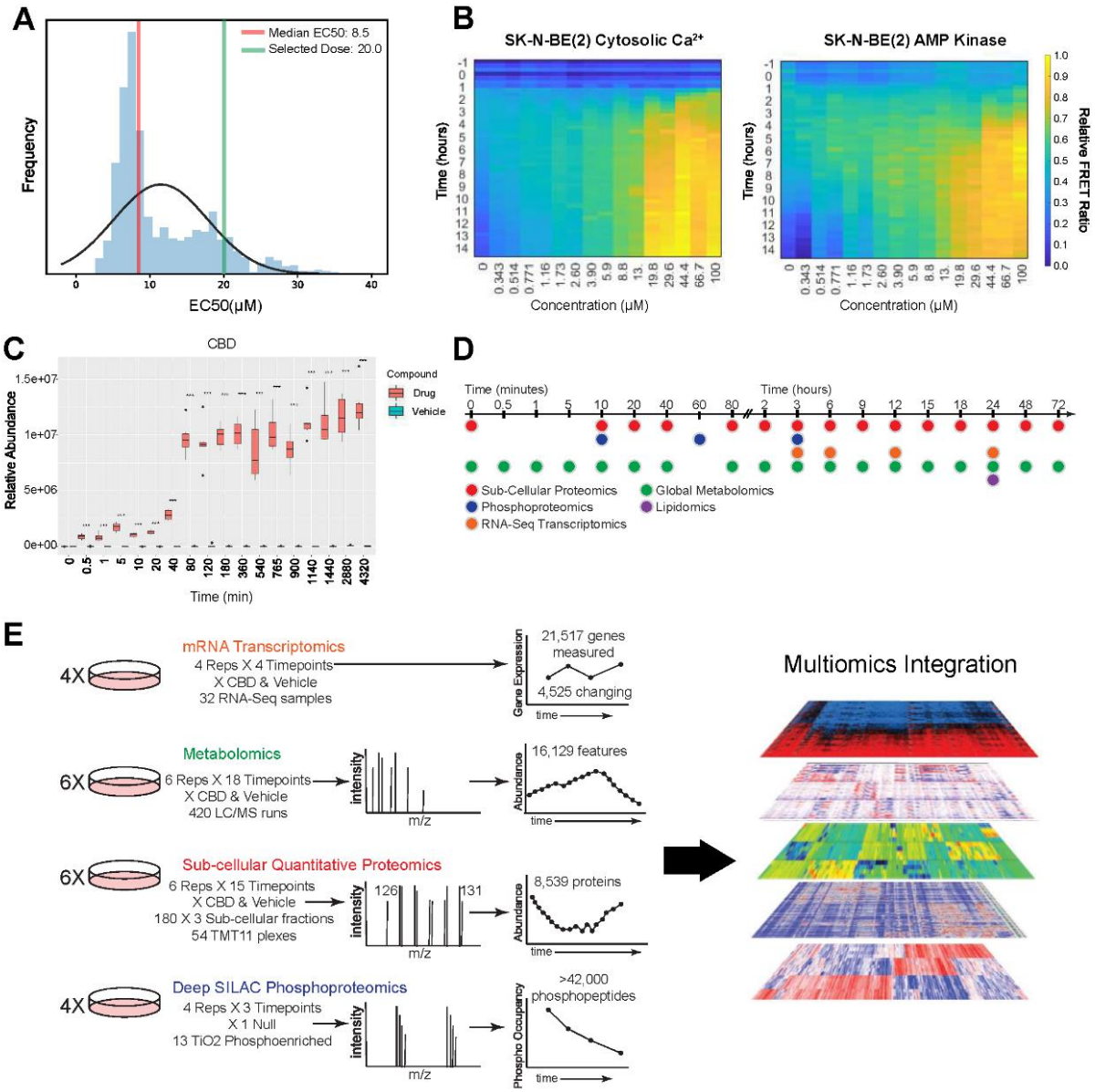

Figure 1. FRET biosensor screening strategy for dose and time selection of multi-omic CBD perturbation analysis. (A) EC_{50} distribution of CBD treatment across all sensors and timepoints (See also Table S1 for list of sensors). Dose response curves were fit to determine EC_{50} values (R^2 values > 0.75) **(B)** Heat maps of FRET biosensor responses to CBD treatment for cytosolic Ca^{2+} and AMPK activity in SK-N-BE(2) cells, displaying FRET ratio over time at CBD doses from 343 nM to 100 µM. **(C)** Relative abundance of CBD over time from metabolomic profiling of SK-N-BE(2) cells treated with 20 µM CBD**. (D,E)** Time course schematic of multi-omic experimental strategy.

BE(2) cells were less sensitive to CBD treatment compared with HaCaT cells, and displayed a higher degree of dose-dependency in FRET sensor activation over time **(Figure S1A).** We therefore selected a CBD dose of 20 µM, and SK-N-BE(2) cells for subsequent multi-omic experiments.

After treatment with 20 µM CBD, the earliest events detected by the biosensors showing dose-dependence were an increase in cytosolic calcium at 3 hours followed closely by AMPK activation **(Figure 1B).** AMPK can be allosterically activated by AMP when AMP:ATP ratios increase, or by the upstream kinases, Ca2+/Calmodulin-dependent protein kinase kinase β (CaMKKβ) and LKB1 (Hawley et al., 2003, 2005; Shaw et al., 2004). CaMKKβ increases the activity of AMPK through direct interactions with its kinase domain, driving downstream secondary calcium signaling events (Hawley et al., 2005; Woods et al., 2005). This calcium FRET sensor response is consistent with previous reports of CBD treatment driving an increase in cytosolic calcium through either TRPM8, TRPV receptors, or Voltage-dependent T type receptors (Ibeas Bih et al., 2015; Rimmerman et al., 2013).

Following dose and cell line selection, we monitored the kinetics of cellular uptake of CBD in SK-N-BE(2) cells. The relative abundance of intracellular CBD was quantified by mass spectrometry in a time course from 30 seconds to 72 hours. CBD was detected in cells as early as 30 seconds but did not reach steady state until 80 minutes post treatment **(Figure 1C).** Based on these kinetics of CBD uptake, we performed a set of multi-omic experiments to examine the temporal response of SK-N-BE(2) cells to CBD treatment, from minutes to days, using global metabolomics, lipidomics, phosphoproteomics, subcellular proteomics, and transcriptomics **(Figure 1D),** resulting in the detection of > 42,000 phosphorylated peptides, 8,359 proteins, 21,517 gene transcripts and 16,129 metabolic features **(Figure 1E)**.

CBD activates AMPK signaling and downstream substrate phosphorylation

We performed SILAC phosphoproteomics to quantify changes in phosphorylation in response to CBD treatment at 10 minutes, 1-hour and 3-hour time points. At the 10-minute time point, only five significantly changing phosphorylation sites were observed ($q < 0.05$ and $|\log2 \text{ ratio}| > 0.5$) **(Figure S2A).** However, the number of significantly changing sites increased to 154 by 1 hour **(Figure 2A)**, mirroring the kinetics of CBD uptake into cells between 40 and 80 minutes **(Figure 1C)**. At both 1 hour and 3-hour timepoints, significantly changing phosphorylation sites were enriched in AMPK signaling proteins. **(Figure 2A, 2B and S2B).** The canonical phosphorylation motif of high confidence AMPK substrates has been identified as L-X-R-X-X-(pS/pT)-X-X-X-L based on peptide amino acid frequencies (Dale et al., 1995; Gwinn et al., 2008; Schaffer et al., 2015). We found that AMPK motifs were significantly enriched in CBD-responsive phosphorylation site sequences at 1- and 3-hours using sequence motif analysis, including L-X-R-X-X-pS and R-X-X-pS-X-X-X-L **(Figure S2C and S2D).** An average of these motifs emerges in the sequence logo at these time points **(Figure 2C and 2D).**

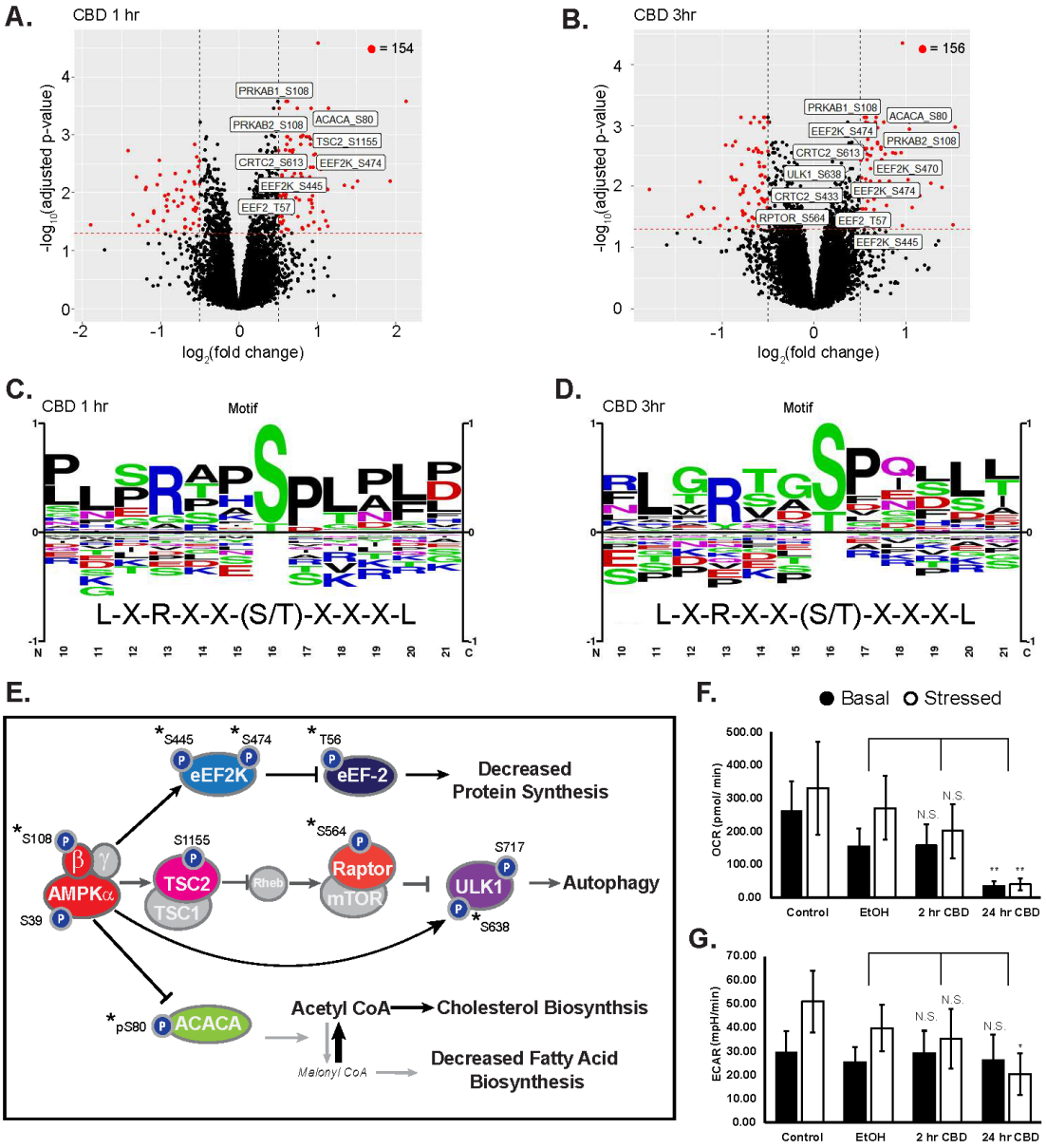

Figure 2. CBD increases phosphorylation of AMPK signaling proteins at early time points. (A-B) Volcano plots of quantified phosphorylation sites at 1 and 3 hours post treatment with 20 µM CBD, showing significance of differential change on y-axis and $\log_2$(CBD/DMSO) ratio on x-axis. Red: adjusted $p < 0.05$, $|\log_2(\text{CBD/DMSO})| > 0.5$. Sites on AMPK proteins involved in AMPK signaling with adjusted p-value < 0.05 are annotated in white boxes. (C- D) Phospho motif enrichment from phosphorylation sites identified as significantly changing in CBD treated cells vs vehicle control at 1- and 3-hours post CBD treatment. The AMPK averaged motif is displayed beneath the sequence logo (Schaffer et al., 2015) (E) Overlay of significantly changing phosphorylated sites onto an AMPK signaling diagram. Asterisks signify phosphorylation sites with a known upstream kinase (F-G) Seahorse extracellular flux measurement of oxygen consumption rate (OCR) and extracellular acidification rate (ECAR), * $p < 0.05$; ** $p < 0.01$. Stressed condition: Oligomycin treatment (1 µM)/ FCCP treatment (1 µM).

Of the observed phosphorylation sites on proteins involved in AMPK signaling, several of the CBD-responsive events are annotated with biological function. We observed increased phosphorylation of S108 within the beta subunit of AMPK at the 1-hour and 3-hour timepoints. Phosphorylation at this site drives a conformational change in the AMPK complex resulting in stabilization of active kinase by preventing dephosphorylation of the activation site at T172 (Li et al., 2015). In agreement with an increase in AMPK activity after 1 hour of CBD treatment, we found increased phosphorylation of S80 on acetyl-CoA Carboxylase (ACACA), a known AMPK phosphorylation site **(Figure 2E)** (Carlson and Kim, 1973; Munday, 2002). ACACA catalyzes the rate-limiting step of fatty acid synthesis, and is deactivated by AMPK phosphorylation of S80. Phosphorylation of ACACA on S80 results in reduced conversion of acetyl-CoA into malonyl-CoA, reducing carbon flux through fatty acid synthesis, and increasing catabolic fatty acid β-oxidation (Fediuc et al., 2006; McFadden and Corl, 2009). In line with these findings, we observed decreased flux of carbon into de novo synthesized fatty acids **(Figure S2E)**. We found significantly decreased levels of short and medium chain, but not long chain acylcarnitines in the CBD-treated cells, indicating that fatty acid mobilization is comparable in the two groups, but more rapidly fluxed through fatty acid β-oxidation upon treatment with CBD **(Figure S2F)**.

We also identified increased phosphorylation of the translation elongation factor, EEF2, on T56 with CBD treatment at 1 and 3 hours. EEF2 T56 phosphorylation is sufficient to inhibit the GTP-dependent ribosomal translocation step during translational elongation, which suggests upstream activity of AMPK and EEF2K (Ryazanov et al., 1988). Together, these observations predict downstream alterations of both protein and fatty acid synthesis rates downstream of AMPK signaling.

Agreement between phosphoproteomics and FRET sensor activity indicated that AMPK is activated by CBD treatment, but did not reveal the mechanism of activation. Upstream activation of AMPK can be initiated through conformational changes driven by cellular AMP:ATP ratio, or through calcium dependent phosphorylation events (Hardie et al., 1999; Woods et al., 2005). To test whether CBD treatment acutely alters cellular energy status, we measured the oxygen consumption rate and extracellular acidification rate of CBD treated cells using a Seahorse extracellular flux assay. Treatment of SK-N-BE(2) cells with 20 μM CBD led to decreased levels of basal oxygen consumption by 24 hours, with little change at 2 hours post-drug treatment **(Figure 2F)**. Basal extracellular acidification rate remained unchanged **(Figure 2G)**. Consistently, we observed comparable rates of lactate production, but decreased carbon flux into TCA cycle metabolites in cells treated with CBD **(Figure S2G).** These results suggest that CBD-treated cells have decreased ATP production by mitochondrial respiration with little to no compensation by glycolysis, which may sustain AMPK activation at late time points. While we do not have direct evidence of the mechanism by which AMPK is activated between 1-3 hours, the most likely explanation is that in the absence of compromised ATP production, calcium influx into the cytoplasm leads to activation of AMPK by calcium activated upstream kinases such as CAMKKβ.

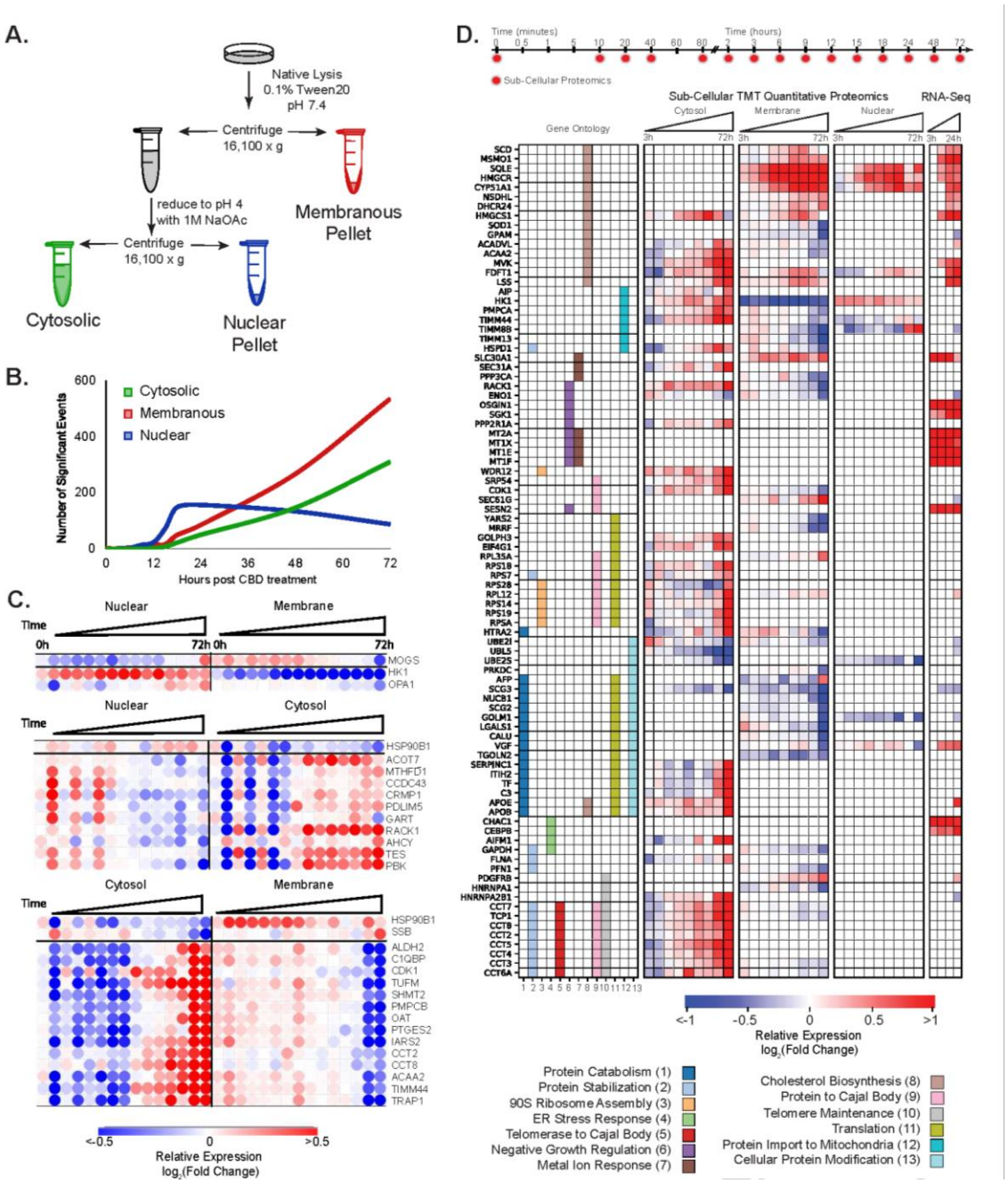

Figure 3. CBD treatment upregulates cholesterol biosynthesis enzymes and translocation of metabolic proteins. (A) Compositionally distinct subcellular proteomic fractions were fractionated by differential centrifugation and pH. The "cytosolic" fraction is enriched in soluble protein, the "nuclear" fraction is enriched in insoluble subnuclear compartments: condensed chromosome, spindles, spliceosomal complex etc., and the "membrane" fraction is enriched in membrane and mitochondrial related proteins. (See also Figure S3C -S3E) (B) Frequency of significantly changing proteomic events over time. (C) Anticorrelated proteins between proteomic fractions over time. PCA dimensionality reduction was used to decrease the impact of noisy signal contribution. Correlation between fractions, r < -0.8 was required. A large proportion of proteins listed above are known to compartmentalize in the mitochondria indicating protein shuttling or mitochondrial detachment/ attachment. (See also Figure S3F) (D) Proteins and mRNA transcripts that change significantly with CBD and map to the indicated gene ontology annotations that showed significant enrichment of differential proteins (Methods).

CBD upregulates transcripts and translocation of proteins involved in cholesterol biosynthesis

To identify time-dependent changes in subcellular localization of proteins, we developed a pH-dependent cell fractionation scheme using differential centrifugation **(Figure 3A; Star Methods).** The resulting 'cytosolic' fraction is enriched in soluble proteins from the cytosol, nucleus as well as various luminal compartments through the cell (mitochondrial, vesical, etc.) **(Figure 3SA).** The first insoluble fraction, labeled as 'membrane', contains proteins from both the mitochondrial and plasma membrane, while the second insoluble fraction is highly enriched in insoluble nuclear components such as condensed chromatin, spindles and nuclear speckles **(Figure S3B and S3C).** Principal component analysis (PCA) of these fractions revealed three compositionally distinct portions of the proteome, with each of these fractions exhibiting a time-dependent separation in response to CBD treatment. **(Figure S3D and S3E).** However, the membranous and nuclear fractions remain very similar in PCA space until 12 hour and later time points, suggesting relatively slow kinetics of protein regulation in response to CBD. Consistent with this observation, the frequency of significant events across fractions are limited at time points prior to 12 hours but increase dramatically to hundreds of proteins at timepoints between 15 to 72 hours. **(Figure 3B).**

Anticorrelation between the time-dependent responses for a protein in different subcellular fractions would be expected for proteins translocating between cellular compartments in response to CBD. To identify potential translocation events, we calculated the Pearson's correlation coefficient between the temporal profiles of each of that protein's subcellular fractions. We found 30 proteins with highly anti-correlated subcellular profiles **(Figure 3C).** Notably, Hexokinase1 (HK1) is observed to decrease in the membrane fraction and increase in the nuclear fraction **(Figure 3C and S3F).** HK1 detachment from the outer mitochondrial membrane results in severely decreased activity to convert glucose to glucose 6-P (Berger et al., 1946). Consistently, CBD-treated cells similarly demonstrated decreased levels of glucose-6-phosphate during later timepoints of CBD treatment **(Figure S3G).** HK1 detachment decouples glycolysis from mitochondrial respiration, and can alter the overall balance of energy metabolism in the cell. This translocation event is consistent with decreased cellular respiration in response to CBD treatment **(Figure 2F)** and previous reports of CBD-induced mitochondrial dysfunction in neuroblastoma cells (Alharris et al., 2019).

To identify CBD-dependent changes in transcript abundance, we performed an RNA-seq experiment, comparing SK-N-BE(2) cells treated with 20 μM CBD or vehicle for 3, 6, 12 and 24 hours. We identified 4,118 differentially expressed genes in CBD treated cells that were significant in at least 1 time point with a false discovery rate (FDR) <1%. 204 of these genes displayed transcript abundances with a |log2 ratio| ≥1 **(Figure 1E)**. To identify potential transcription factor specific responses that explain mRNA transcript changes, we performed upstream regulator analysis on significantly changing transcripts (Krämer et al., 2014). The most enriched transcription factors for increasing transcripts shared oxidative stress as a stimulus and included ATF4, NFE2L2, SP1 **(Figure S3H)** (Blais et al., 2004; Dasari et al., 2006; Venugopal and Jaiswal, 1998; Wang and Semenza, 1993). Along similar time scales, CBD-treated cells showed an accumulation of the principal cellular antioxidant glutathione, indicating an upregulation

in oxidative stress response **(Figure S3G).**

We merged differentially expressed transcript and protein identifications by gene name and assigned gene ontology annotations using REVIGO pathway analysis **(Figure 3D)** (Supek et al., 2011). CBD responsive events were enriched in translation, ER stress response, metal ion response, and cholesterol biosynthesis (adj. $p < 0.01$). While many of these annotations are supported by either the transcriptome or proteome, dysregulation of cholesterol metabolism is supported by both. Within the cholesterol biosynthetic pathway ontology enrichment, 17 proteins displayed significant abundance changes that increased over time, including several key regulatory proteins. The rate limiting enzyme in cholesterol synthesis, HMGCR, increased as much as 303%, with increased transcript abundance by 6 hours. Negative regulators of this rate limiting enzyme were observed to decrease, including a 40% decrease in SOD1, consistent with decreased repression of *HMGCR* transcription (De Felice et al., 2004). The enzyme catalyzing the conversion of desmosterol into cholesterol in the terminal step in cholesterol biosynthesis, DHCR24, increased by 43% on the protein level in the "membrane" fraction (**Figure 3D**). Together, the proteomic and transcriptomic data point to a concerted response in cholesterol homeostasis pathways in response to CBD treatment, and predict an upregulation of cholesterol biosynthesis capacity.

CBD treatment results in accumulation of cholesterol biosynthesis intermediates and esterified cholesterol

Proteomic and transcriptomic analyses revealed a concerted CBD-induced upregulation of cholesterol biosynthesis machinery. These findings raised the question of whether CBD treatment leads to alterations in lipid and cholesterol metabolism (the latter pathway depicted in **Figure 4A**). We used mass spectrometry-based lipidomics to quantify the effect of CBD on lipids and sterols. Vehicle and CBD exposed cells were pulse labeled with [U-$^{13}C_6$]-D-Glucose for 24 hours and harvested using methanol extraction. Cholesterol biosynthetic flux was quantified by mass spectrometry analysis of ^{13}C incorporation into biosynthetic intermediates. We found that cholesterol precursors accumulated in CBD exposed cells **(Figure 4B and S4A)**, while labeled and total cholesterol itself decreased modestly (**Figure 4B and S4B**). This effect of CBD on total cellular cholesterol was confirmed using an Amplex Red cholesterol assay (**Figure S4C**).

Intracellular cholesterol is stored in lipid droplets after esterification with long-chain fatty acids by ER-resident enzymes (Brown et al., 1980). We detected accumulation of multiple species of cholesteryl esters with various chain lengths and acyl-chain saturation **(Figure 4C)**. Upregulation of cholesterol biosynthesis enzymes, together with increased abundance of metabolic precursors, suggest that CBD leads to increased production and storage of cholesterol.

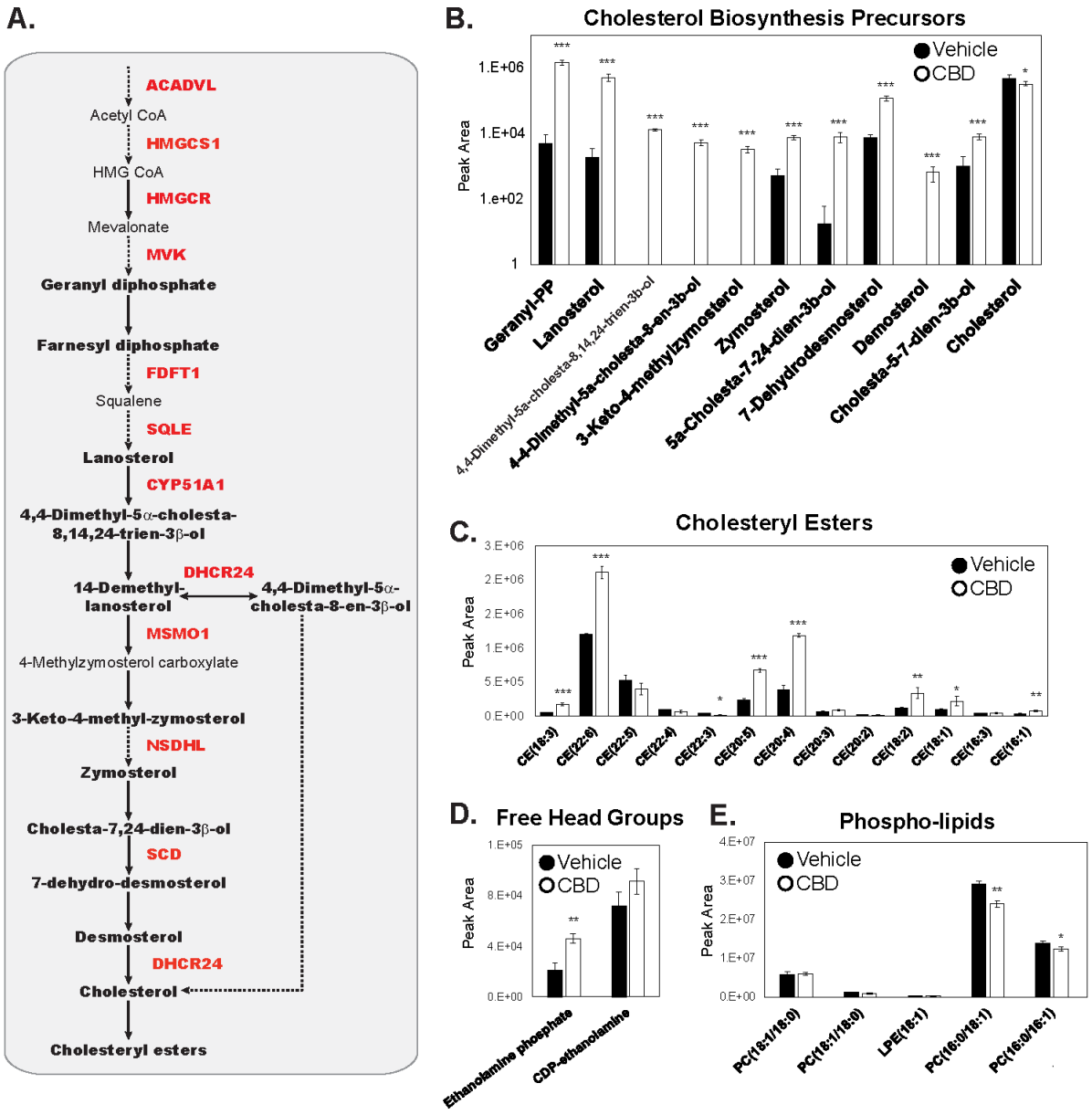

Figure 4. Cholesterol biosynthesis precursors and cholesterol esters accumulate upon CBD treatment. (A) Pathway diagram of cholesterol biosynthesis. Quantified metabolic intermediates are outlined in black bold, enzymes showing significant increase over time with CBD in proteomic analysis are shown bold red (Figure 3D). Dashed arrows indicate multiple intermediate steps that were not identified in the pathway. (B) D-glucose (U-$^{13}C_6$) metabolically labeled cholesterol biosynthesis precursors at 24 hours post 20 μM CBD treatment. (Student's T Test : *p< 0.05, **p<0.01, ***p<0.001) (See also Figure S4) (C-E) Total abundance of lipids quantified by LC/MS/MS from lipid extracts of SK-N-BE(2) cells treated with vehicle or 20 μM CBD. Cholesteryl esters (CE), free head groups and phospholipids identified by mass spectrometry are displayed. Phosphatidylcholine(PC); Phosphatidylethanolamine (PE); lysophosphatidylethanolamine (LPE) (Student's t-test: *p< 0.05, **p<0.01, ***p<0.001).

Due to the requirement of acyl-CoA precursors in cholesterol esterification (Chang et al., 2009), we surveyed our dataset for evidence of fatty acid utilization. We found that CBD treatment led to the accumulation of metabolites derived from phospholipid head-groups (**Figure 4D and S4D**), including ethanolamine phosphate, a product of sphingosine catabolism via the enzyme S1P lyase (SGPL1) (Serra and Saba, 2010). These data suggest that both free and SGPL1-generated fatty acids may be utilized for cholesterol esterification. We also surveyed the cellular abundance of all detectable species of phosphatidylcholine and phosphatidylethanolamine in cell extracts and found a variety of phospholipids that display reduced abundance in CBD treated versus vehicle treated cells (**Figure 4E**). These observations are consistent with previous studies showing catabolic breakdown of phospholipids upstream of SGPL1 activity (Aguilar and Saba, 2012). Thus, we found multiple lines of evidence consistent with activation of cholesterol esterification in the CBD response.

CBD increases storage and transport of cholesterol

Cholesterol is a critical structural component of cellular membranes. Alterations in cholesterol abundance can lead to severe cellular phenotypes that include mitochondrial dysfunction and apoptosis (Zhao et al., 2010). Disruption in cholesterol trafficking is a hallmark of Niemann-Pick Type C disease (Chang et al., 2005), and can drive sodium channel-mediated inflammatory pain in animal models (Amsalem et al., 2018). To explore the phenotypic implications of CBD disruption of cholesterol homeostasis, we tested whether CBD-induced cell death required upregulated cholesterol synthesis. Earlier experiments indicated that 40 µM CBD can induce cell death after 24 hours in SK-N-BE(2) cells (**Figure 5A**). SK-N-BE(2) cells were exposed to increasing concentrations of CBD in the presence or absence of the cholesterol biosynthesis inhibitor, atorvastatin, and analyzed for apoptosis using CellEvent caspase 3/7 dyes and live-cell fluorescence imaging. At 15 hours, 100 µM CBD leads to apoptosis of 50% of SK-N-BE(2) cells. Co-treatment of SK-N-BE(2) cells with CBD and atorvastatin reduced apoptosis by approximately 2-fold (**Figure 5B**). This atorvastatin-dependent rescue of CBD-induced apoptosis was far more pronounced in human HaCaT keratinocytes (**Figure S5A**), which are highly sensitive to cholesterol perturbation (Bang et al., 2005). Further, CBD exposed SK-N-BE(2) and HaCaT cells show an increase in apoptosis with increasing concentrations of a soluble form of cholesterol, 25-hydroxycholesterol (25HC) (**Figure 5C, and S5B).** Together, these results show that CBD sensitizes cells to apoptosis when challenged with excess cholesterol, either from endogenously synthesized or exogenous pools.

We next determined the impact of perturbations to cholesterol transport and storage on CBD-induced apoptosis. We measured apoptosis in SK-N-BE(2) and HEK293T cells treated with CBD and sublethal doses of 25HC (15 µg/ml), in combination with a cholesterol transport inhibitor (NPC1 inhibitor U18666A, 10 µM), or an inhibitor of acyl-coenzyme A cholesterol O-acyltransferase (ACAT), an enzyme required for esterification and intracellular storage of cholesterol (VULM 1457, 5 µM). Both compounds sensitized cells to apoptosis when CBD was present, which was more pronounced when cells were also challenged with 25HC (**Figure 5D and 5E**). VULM and U18666A treatment alone did not lead to increases in apoptosis. These results

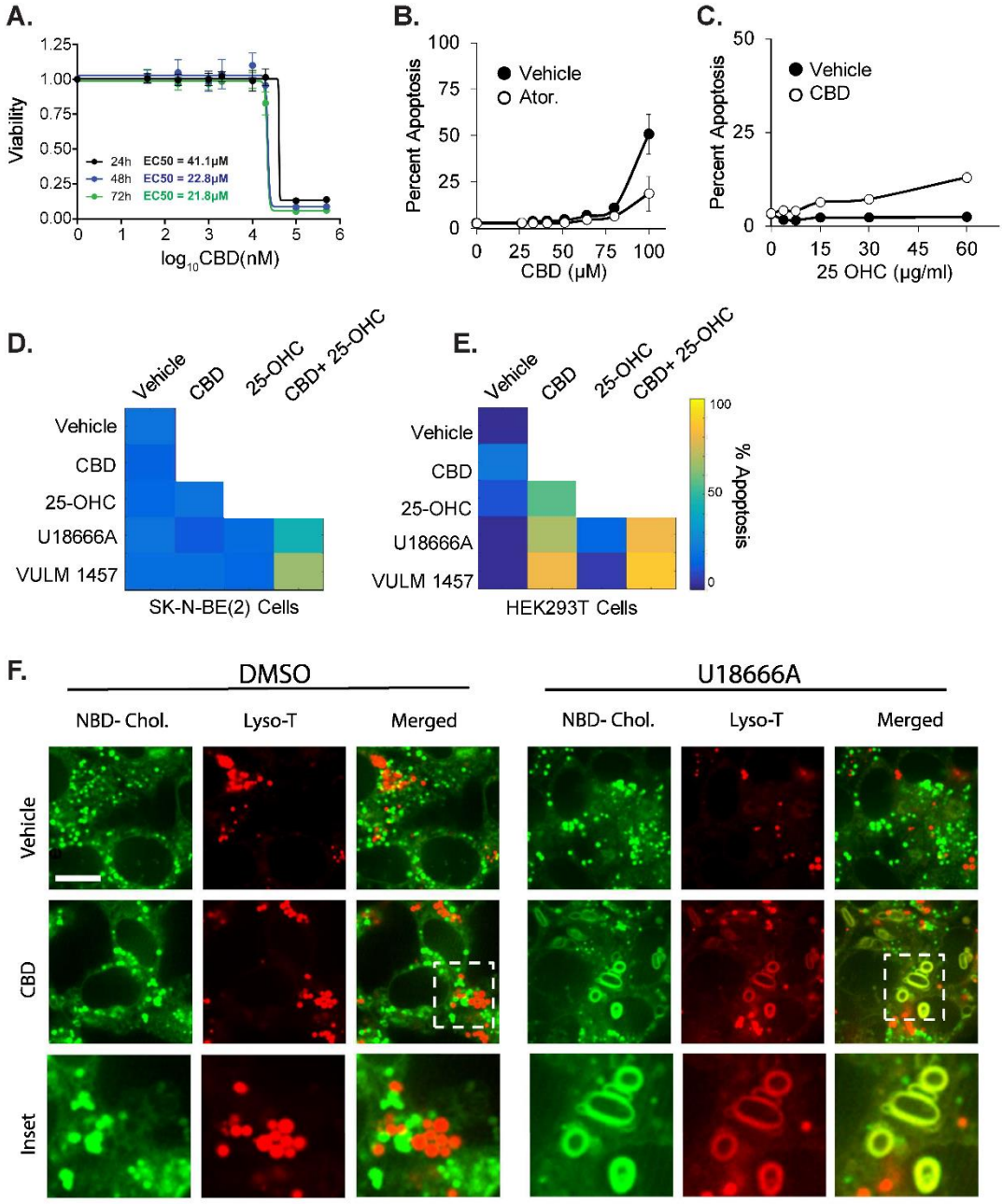

Figure 5. CBD induced apoptosis is rescued by inhibitors of cholesterol synthesis and increased by inhibitors of cholesterol transport and storage. (A) CBD was assessed for cytotoxicity in SK-N-BE(2) cells across increasing doses of CBD at 24, 48 and 72 hours by CellTiter-Glo luminescent assay. (B-E) SK-N-BE(2) or HEK293T cells were assessed for apoptosis at 24 hours using live cell microscopy using a resazurin based fluorometric cell viability stain. Cells were treated with 10 µM atorvastatin and exposed to increasing doses of CBD in B. 20 µM CBD and exposure to increasing doses of 25-OH cholesterol in C, and combinations of 20 µM CBD, 10 µM U18666A, 5µM VULM and 15µg/ ml 25- OH Cholesterol at 48 hours in D-E. Apoptosis displayed in a heatmap for each condition. (See also Figure S5) (F) Live cell confocal microscopy of SK-N-BE(2) with NBD-Cholesterol (Green) and a lysosomal dye Lyso-T (Red). Cholesterol subcellular distribution was examined upon exposure of cells to 20 µM CBD and/ or 10 µM U18666A. Scale bar: 3 µM

indicate that interfering with cholesterol transport or cholesterol storage sensitize cells treated with CBD to apoptosis.

One possible explanation for why CBD sensitizes cells to inhibitors of cholesterol trafficking and storage is that CBD increases the flux of cholesterol transport from the plasma membrane through the endosomal-lysosomal pathway. In support of this hypothesis, we observed increases in apolipoproteins B and E (APOB, APOE) abundance in the cytosol-enriched fraction. APOB/E are lipoprotein components of cholesterol-containing low density lipoprotein particles required for cellular uptake of cholesterol **(Figure 3D)**. When cholesterol import through low density lipoprotein receptors (LDLR) is activated, and 25HC is supplied in excess, the inability to efficiently store cholesterol may cause subcellular accumulation of cholesterol in organelles that normally maintain low cholesterol levels. To examine this possibility, we visualized lysosomes (lysotracker dye) and cholesterol (NBD-cholesterol) in vehicle and CBD treated SK-N-BE(2) cells with live cell confocal microscopy.

In cells treated with either CBD or U18666A alone, puncta stained with lysotracker and NBD-cholesterol showed distinct spatial separation within cells. In contrast, co-treatment with CBD and U18666A led to formation of enlarged, membranous organelles co-stained with lysotracker and NBD-cholesterol, with a central unstained lumen-like area (**Figure 5F**). Morphologically similar structures have been reported in models of Niemann-Pick type C (NPC) disease, in which cholesterol accumulates in enlarged lamellar inclusions with components of lysosomes and endosomes, leading to a toxic cycle of enhanced cholesterol synthesis and intracellular accumulation (Demais et al., 2016; Höglinger et al., 2019). Sensitization of cells by CBD to drugs that disrupt intracellular trafficking of cholesterol, combined with our observations that CBD increases endogenous cholesterol biosynthesis and stimulates cholesterol esterification (**Figures 5D,E and 4B,C**), support a model where CBD increases transport of plasma membrane cholesterol through the endosomal-lysosomal pathway to intracellular compartments where it is esterified and sequestered, escaping ER-resident cholesterol sensing machinery (Cheng et al., 1995; Lange et al., 1999).

CBD incorporates into membrane compartments altering cholesterol orientation and lateral diffusion

Subcellular fractionation of SK-N-BE(2) cells treated with CBD for 24 hours showed that CBD is concentrated primarily at the plasma membrane, with lower levels detected in ER and nuclear membranes (**Figure 6A**). CBD accumulation in the plasma membrane, and our evidence that CBD activates the internalization of plasma membrane cholesterol, suggests that CBD alters cholesterol orientation and availability within the plasma membrane. To measure the effect of CBD on cholesterol chemical activity, we measured the enzymatic oxidation rate of cholesterol to 5-cholesten-3-one by cholesterol oxidase in small unilamellar vesicles (SUVs). Cholesterol oxidase has been shown to sense alterations of lipid bilayer structure and cholesterol orientation (Ahn and Sampson, 2004), and could reveal CBD-dependent alterations in cholesterol orientation in membranes. Titration of CBD into cholesterol-containing SUVs increased the initial reaction rate of cholesterol oxidase in a manner proportional to CBD concentration (**Figure 6B and S6A**).

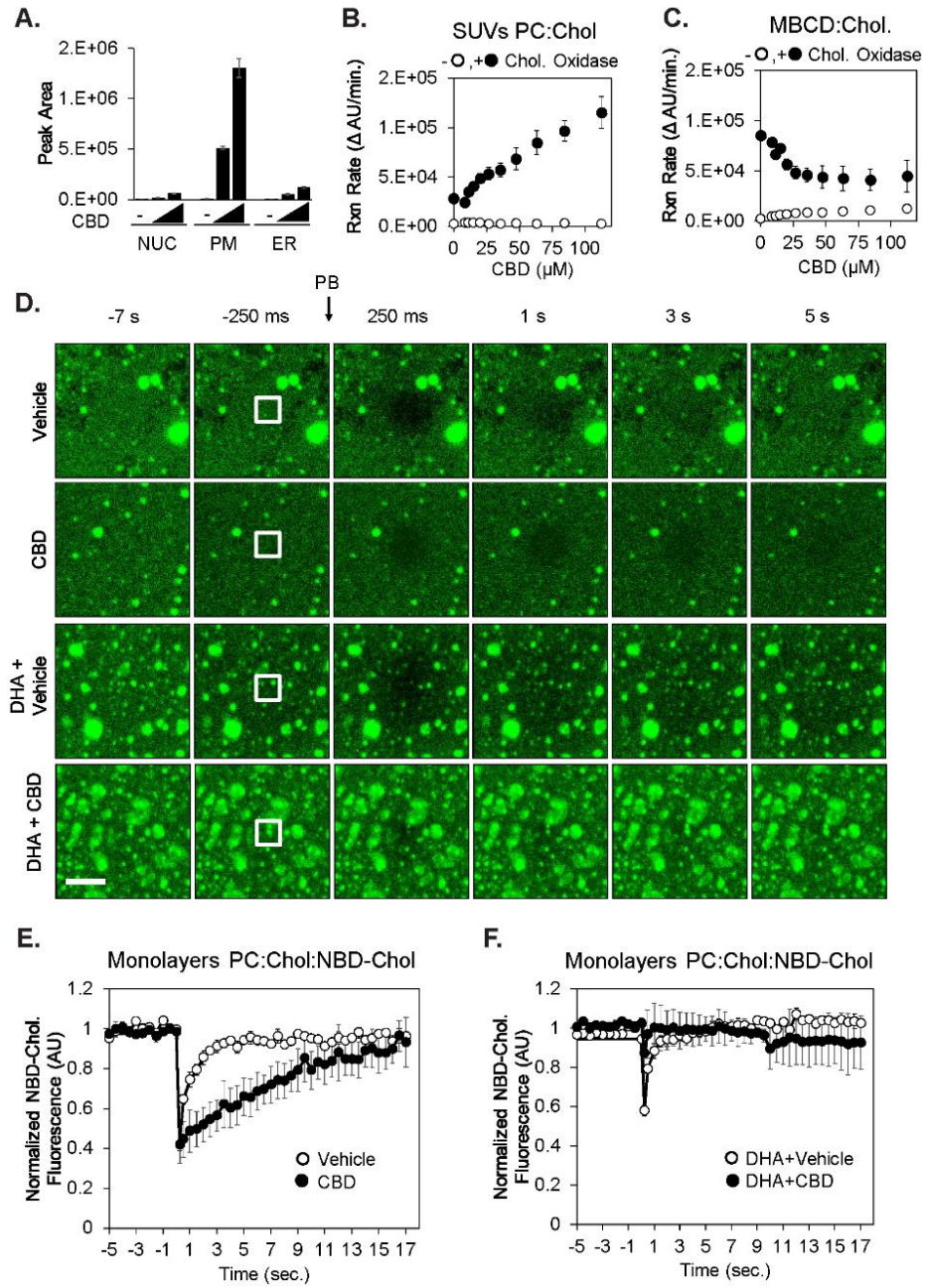

Figure 6. CBD incorporates into membranes, increases cholesterol chemical activity, and reduces lateral diffusion of cholesterol. (A) Ethanol extracts of subcellular fractions of SK-N-BE(2) cells exposed to 0, 20 and 40 μM CBD for 24 hr were analyzed for CBD using LC-MS. (B) Synthetic small unilamellar vesicles (SUVs-molar ratio: phosphatidylcholine:cholesterol:NBD cholesterol: 78:20:2 (n/n%) were used as a source of cholesterol in a fluorogenic cholesterol oxidase reaction to determine the effect of CBD on initial reaction rate. (C) Identical experiments were performed with cholesterol complexed to methyl beta cyclodextrin (MBCD), without SUVs present (D) Synthetic membrane monolayers containing NBD-cholesterol were adsorbed to borosilicate glass and used in fluorescent recovery after photobleaching (FRAP) experiments following exposure to either CBD (60 μM) and/or DHA (20 μM). Scale bar is 2.5 μm. Quantified fluorescence recovery after photobleaching is displayed in (E) and (F) (n=3).

The dose-dependent increase in cholesterol oxidase activity by CBD requires cholesterol localized in membranes, as freely soluble 25HC (**Figure S6B**), and soluble complexes of cholesterol and methyl beta cyclodextrin (MBCD), showed no dose dependence on CBD (**Figure 6C**)**.** We repeated this experiment in a complex membrane environment using vesicles derived from ER membranes, and again observed a concentration dependent increase in cholesterol oxidase activity in response to CBD (**Figure S6C).** Together, these data provide evidence that CBD incorporates into membranes and alters cholesterol accessibility, likely by altering cholesterol orientation within the membrane to make the hydroxyl moiety more solvent accessible.

The ability of cholesterol oxidase assays to reveal alterations in lipid order has been previously reported in studies noting that cholesterol oxidase can preferentially target specialized ordered lipid domains known as caveolae (Ortegren et al., 2004; Smart et al., 1994). Our results showing that CBD affects cholesterol activity in both synthetic and cell derived ER membranes implies that CBD may contribute to increased lipid order. A hallmark of increased lipid order is a decrease in lateral diffusion of lipids (Ferreri, 2005; Lindblom and Orädd, 2009). We measured the effect of CBD on the lateral diffusion of fluorescently labelled cholesterol (NBD-cholesterol) in synthetic membrane monolayers. SUVs containing 20% (n/n%) of cholesterol and 2% (n/n%) NBD-cholesterol were deposited on glass-bottom multiwell imaging plates, followed by ultra-sonification. Recovery kinetics of fluorescent cholesterol were monitored in the presence of vehicle or CBD using fluorescence recovery after photobleaching (FRAP) **(Figure 6D)**. CBD significantly reduced the recovery of fluorescence in the photobleached monolayer area relative to vehicle control (**Figure 6D and 6E**), suggesting that CBD slows the lateral diffusion of fluorescent cholesterol. This effect of CBD on lateral diffusion could be rescued with simultaneous treatment of the docosahexaenoic acid (DHA), a known disrupter of lipid order (**Figures 6D and 6F**).

Our FRAP experiments demonstrate that DHA and CBD have opposing effects on the lateral diffusion of fluorescently labelled cholesterol in synthetic membranes. Although this implies that CBD increases lipid order and that DHA decreases lipid order, it remains unclear how these biophysical effects of CBD and DHA on cholesterol impact cellular physiology. Esterification of DHA into membrane phospholipids results in remodeling of sphingolipid/ cholesterol-enriched lipid rafts, a known hub for apoptosis signaling (George and Wu, 2012; Wassall et al., 2018). To determine whether CBD and DHA also have opposing effects in a cellular context, we quantified the effect of CBD and DHA on cholesterol-dependent apoptosis. DHA treatment induced apoptosis in both HEK293T and SK-N-BE(2) cells in a dose dependent manner (**Figure S6D and S6E**), consistent with previous studies (Geng et al., 2018; Serini et al., 2008; Shin et al., 2013; Sun et al., 2013). Importantly, this DHA-induced apoptosis proved to be cholesterol dependent, as simultaneous treatment with DHA and the cholesterol sequestering agent, MBCD, delayed apoptosis in HEK293T cells, and fully rescued apoptosis in SK-N-BE(2) cells (**Figure S6D and S6E**). Similarly, CBD treatment (6.25 µM) rescued the apoptotic effects of DHA in both HEK293T and SK-N-BE(2) cells at 48 hours (**Figure S6D and S6E)**. These data indicate that CBD and DHA have opposing effects on cellular membrane structure and induction of apoptosis, both of which are cholesterol-dependent, but the connection between these two processes remain unclear. Previous

observations that CBD induces lipid raft coalescence in mouse microglial cells (Wu et al., 2012) suggests that CBD may alter lipid raft structure in a manner that frees lipid raft associated cholesterol to internalization mechanisms.

Consistent with CBD alterations in cholesterol orientation, we found that CBD sensitized live cells to the chemical agent filipin. Filipin is a highly fluorescent probe known to bind cholesterol and disrupt nearby lipid ordering, resulting in permeabilization of membranes. Cells pretreated with 20 µM CBD for 24 hours were preferentially permeabilized by filipin relative to vehicle control **(Figure S6F)**, further supporting a CBD-dependent alteration in plasma membrane structure and cholesterol orientation. This data suggests that CBD either directly increases cholesterol availability to filipin, or destabilizes the membrane, thereby contributing to the membrane disruption effects of filipin.

Discussion

Although clinical and preclinical evidence point to CBD as a promising therapeutic compound for epilepsy, the cellular targets that mediate its effects in humans remain largely unknown. In this study, we found that CBD elicits a diverse and pleiotropic effect on human cells, using an unbiased profiling strategy of transcriptomics, subcellular proteomics, phosphoproteomics, metabolomics, lipidomics, isotope tracing and live cell microscopy. Our data suggest that CBD integrates into cellular membranes and alters cholesterol orientation within the phospholipid environment. Partitioning of CBD into model membranes increased lipid order, decreased lateral diffusion, and altered cholesterol availability to the enzyme cholesterol oxidase, and would predict that CBD alters the biophysical properties of cellular membranes membrane, with consequent effects on diverse membrane proteins and their downstream targets.

We found that CBD treatment led to increased cytosolic calcium within 2 hours in human neuroblastoma and keratinocyte cells. AMPK activity followed the observed increase in calcium, suggesting upstream activation of AMPK by the calcium-dependent kinase CAMKKβ. Compromised ATP generation by mitochondrial respiration may sustain AMPK activation after 24 hours, as suggested by our Seahorse analysis. Increased AMPK activity, and increased phosphorylation of its substrate ACACA, predicted reduced fatty acid synthesis and altered Acetyl-CoA metabolism, which was confirmed by flux metabolomics. Upregulation of cholesterol biosynthesis on proteome, transcriptome and metabolomic levels occured as early as 3 hours and was sustained up to 72 hours. As acetyl-CoA is precursor of cholesterol, the increase in cholesterol biosynthesis precursors are consistent with acetyl-CoA supporting this flux. Parallel to upregulation of cholesterol biosynthesis, increased cholesterol ester import occurs through the LDLR-endocytic pathway, resulting in increased transport of cholesterol through the lysosome. Increased stress on cholesterol regulatory processes, combined with compromised cellular energetics driven by CBD may contribute to increased apoptosis in CBD-treated cells. We propose that cholesterol is the primary pharmacological effector of CBD in our human cell systems, rather than any given protein receptor or target.

CBD integrates into cellular membranes and increases lipid order

Despite multiple lines of preclinical evidence outlining a wide array of phenotypic effects of CBD (De Filippis et al., 2011; Esposito et al., 2011; Hinz and Ramer, 2019; Kenyon et al., 2018; Massi et al., 2013; Pan et al., 2009; Rajesh et al., 2010), the molecular targets that underlie these effects remain unknown. Our *in vitro* data with model membranes demonstrate that CBD causes increased accessibility of cholesterol to cholesterol oxidase, presumably through tight packing of cholesterol, CBD and possibly phosphatidylcholine (**Figure 6B**). This result is surprising because it suggests that CBD can induce ordered domains in the complete absence of sphingolipids, which are historically used in formulations of model membranes for studying lipid order (Schroeder et al., 1994; Silvius, 2003). Nevertheless, we detected the same behavior of cholesterol in CBD treated ER membranes derived from subcellular fractionation of living cells (**Figure S6C**), which implies that this ordering effect can also occur in cellular membranes. Consistent with the effect of CBD on cholesterol orientation and packing, we demonstrate that fluorescent cholesterol displays diminished lateral diffusion in response to CBD exposure to synthetic membranes, and that this effect opposes, and can be reversed by, the polyunsaturated lipid DHA (**Figure 6D-F**). Since diminished lateral diffusion of lipids has been previously shown to be a hallmark of increased lipid order, this data represents a second line of evidence for CBD induced order in membranes. Additionally, the opposing effect between CBD and DHA on model membranes was recapitulated in living cells in an opposing effect on apoptosis (**Figure 7 B, C**), which strengthens the case that CBD can affect the lipid order in cholesterol containing membranes in living cells.

CBD has previously been reported to induce apoptosis in murine primary microglial cells in a manner that was rescued by MBCD (Wu et al., 2012). MBCD is a selective agent for the depletion of cholesterol from membranes by binding cholesterol within its hydrophobic core (Kilsdonk et al., 1995; Klein et al., 1995). In this model, CBD treatment enriched the membrane with large regions of lipid ordered domains marked by gangliosides and caveolin-1. This lipid raft coalescence was also rescued by MBCD treatment, providing a consistent model when combined with our data for the cholesterol dependency of CBD-induced apoptosis. Within cells, lipid ordered domains (also referred to as lipid rafts) are 10-120 nm wide transient domains in membrane structures where tight packing of cholesterol, sphingolipids and GPI-anchored proteins allow for activation of signaling cascades via the increased proximity of specific proteins (Lingwood and Simons, 2010). These ordered domains have been implicated in generating receptor signaling, assembly of endocytic machinery and endocytosis, and regulation of intracellular calcium. Our data suggest that direct alterations in cholesterol orientation and packing could underlie previously observed alterations in lipid raft stability and size. Further, disruption of these lipid rafts is consistent with downstream changes in calcium regulation, as well as cell death signaling as observed by FRET sensor and caspase apoptosis assays presented here **(Figure 1B and 5A)** (George and Wu, 2012; Liu et al., 2006; Pani and Singh, 2009).

Concordance of multi-omic data points to CBD disruption of cholesterol homeostasis

Integration of our transcriptomics, metabolomics, and proteomics data provided multiple lines of evidence for the disruption of cellular cholesterol homeostasis by the uptake of CBD into human cell lines. Multiple aspects of cholesterol regulation were dysregulated by CBD: cholesterol biosynthesis (**Figure 3D and 4B**), transport (**Figure 3D and 5F**), and storage (**Figure 4C**). All three -omics methods provided evidence for perturbed cholesterol biosynthesis. For instance, transcriptomics and proteomics reported transcriptional activation and protein accumulation of the rate limiting enzyme in the biosynthetic pathway of cholesterol, HMGCR (**Figure 3D**). Increased HMGCR protein production is a canonical response to decreased cholesterol levels in the ER, where cholesterol is sensed through the SREBP-SCAP axis (Brown and Goldstein, 1997). Consistent with this observation, we found that cholesterol precursors accumulate in CBD-treated cells (**Figure 3B, S3A**), with a modest decrease in total cholesterol (**Figure 3B, S3A, S3B**) and a large increase in cholesterol esters.

Paradoxically, we found that CBD triggered the upregulation of cholesterol biosynthesis enzymes, despite evidence showing only modest changes in total cholesterol, and increased levels of cholesterol esters, which would normally result in downregulation of cholesterol biosynthesis by the ER-resident SREBP sensing machinery (Brown and Goldstein, 1997). These results suggest that in the presence of CBD, the ER is unable to accurately sense the abundance of cholesterol at the plasma membrane, and as a result, generates unneeded cholesterol that is esterified due to excessive intracellular accumulation. GRAM domain proteins that localize to plasma membrane- ER contact sites, bind and transport specific lipids between the two membranes (Besprozvannaya et al., 2018). Within this family, GRAMD1s sense and bind the ‘accessible’ pool of cholesterol that is not currently complexed with other lipid species, and transports it to the ER (Naito et al., 2019). The pools of cholesterol that are either ‘accessible’ or ‘inaccessible/sequestered’ are regulated by the domains they associate with, and are frequently driven by sphingomyelin and phospholipid association (Das et al., 2014; Lange et al., 2013; Sokolov and Radhakrishnan, 2010). CBD driven alterations of cholesterol orientation and decreased lateral diffusion presented here, together with previously reported CBD-dependent increases in lipid raft stability and size, provide strong evidence that the pool of ‘sequestered cholesterol’ is increased in CBD treated conditions. However, specific investigation of GRAMD1 sensing and partitioning of CBD and cholesterol within the ER membrane will need to be investigated in future studies.

The effects on cholesterol homeostasis in therapeutic applications of CBD

Our study demonstrates a global profiling strategy to identify key mechanistic components in the CBD response, classify those components into broad biological processes, and identify CBD as an efficient modulator of lipid order from which the downstream effects originate. Our findings that CBD leads to disruption in cholesterol and lipid homeostasis has broad implications on the mechanistic underpinnings of the clinical effects of CBD in a wide array of diseases. Transmembrane proteins known to be regulated through lipid ordered domains have been implicated in many of the diseases for which CBD has been proposed as a therapeutic. These include

inflammatory disorders, Alzheimer's disease, cancer (Gianfrancesco et al., 2018; Hsu et al., 2018; Mollinedo and Gajate, 2015; Pirmoradi et al., 2019; Staneva et al., 2018). Many of the targets of CBD proposed to underlie its efficacy as an anti-convulsant are membrane proteins, including TRPV1, GPR55, and adenosine transport proteins (Bisogno et al., 2001; Liou et al., 2008; Ryberg et al., 2007). CBD inhibits ion currents from many structurally diverse voltage-gated ion channels at similar micromolar concentrations, and with a high degree of cooperativity, suggesting that CBD acts indirectly on ion channels through perturbation of membrane structure (Ghovanloo et al., 2018). Moving forward, it will be important to determine the role of lipid order and cholesterol orientation in the mediation of CBD-induced effects in models of generalized seizures.

Importantly, our study suggests that not all CBD effects on cells are therapeutically beneficial, and that high dose use of CBD may lead to cholesterol-dependent side effects in certain cell types that rely on high levels of cholesterol synthesis or import. We demonstrated that CBD dependent apoptosis is heavily dependent on the cholesterol status of cells (**Figure 5B, 5C, S5A and S5B**). As most of the cholesterol in humans is synthesized in hepatic cells, we predict that many of the side effects of heavy CBD consumption may occur in the liver. Indeed, some clinical evidence of the adverse side effects of CBD in the liver has begun to emerge. Long term CBD use is associated with elevated aminotransferase activity (Gaston et al., 2017), a hallmark of liver injury (Giannini et al., 2005). Our data predict that CBD use may interact adversely with certain dietary behaviors that elevate blood cholesterol, as the combination of cholesterol/ hydroxycholesterol and CBD is toxic to a cell line derived from skin (HaCaT cells), brain (SK-N-BE(2) cells), and kidney (HEK293T cells) (**Figures 5D, 5E, S5B**). Further, our results show that CBD in combination with U18666A disrupts cholesterol trafficking through lysosomes, raising the question of whether CBD use might increase the risk of toxicity in patients with Niemann-Pick Disease, which harbor mutations in NPC1, the target of U18666A (Lu et al., 2015).

By combining unbiased multi-omic profiling and biosensor activity screening, we identified an unexpected pleiotropy of CBD action in human cell lines. Pharmacological pleiotropy is a well-known phenomenon associated with steroid drugs such as statins (Davignon, 2004), which target cholesterol biosynthesis, and raises an important question of whether CBD acts directly through perturbation of membrane structure and cholesterol content, or through inhibition of proteins involved in cholesterol trafficking and synthesis. Our data supports a model where CBD partitions rapidly into cellular membranes, disrupting the distribution of cholesterol in lipid rafts, leading to compromised barrier function of the ER and PM, and dysregulated sensing and biosynthesis of cholesterol.

Acknowledgements:

The authors acknowledge the BioFrontiers Computing Core at the University of Colorado Boulder for providing High Performance Computing resources (NIH 1S10OD012300) supported by BioFrontiers IT. The imaging work was performed at the BioFrontiers Institute Advanced Light Microscopy Core. The Molecular Devices ImageXpress was supported by NIH grant 1S10RR026680-01A1. Laser scanning

confocal microscopy was supported by NIST-CU Cooperative Agreement award number 70NANB15H226. This work was supported by a DARPA cooperative agreement, 13-34-RTA-FP-007, to WMO, MHBS, XL, and AD.

Authorship Contributions:

Conceptualization: W.O., X.L., and D.A.C.; Formal Analysis: J.J., S.C. and S.E.G.; Funding Acquisition: W.O., M.H.B.S and X.L. Investigation: X.L., W.O., D.A.C., S.E.G., C.E., T.N., K.W., K.A.B., H.S., Z.P., J.R.H., and A.R.; Methodology: X.L., W.O., D.A.C., C.E., J.J. and S.C.; Project Administration: W.O.; Resources (purified hemp-derived cannabidiol): R.S.; Supervision: M.H.B.S., A.D., X.L. and W.O.; Visualization: W.O., S.E.G., D.A.C., T.N., J.J., S.C., C.E. and E.B.; Writing - Original Draft: S.E.G., D.A.C. and W.O.; Writing - Review & Editing: S.E.G. and W.O.

Declaration of Interests:

XL, DC and WO are patent holders of PCT WO2019246632A1, and XL, DC, WO and EB are patent holders of PCT WO2019118837A1. Both patents are related to this work. Unrelated to the contents of this manuscript, AD and TN are founders of Omix Technologies Inc, D.C. is the founder of Biooloomics, Inc, and RS is the founder of Sievers Infinity LLC.

STAR Methods:

Compound Preparation:

CBD was derived from domestically grown industrial hemp that was cultivated and purified by Sievers Infinity, LLC, Colorado-owned corporation, registered with the Colorado Department of Agriculture (CDA) to grow and cultivate industrial hemp (CDA # 69096). The purified hemp-derived material was characterized by mass spectrometry, X-ray diffraction, differential scanning calorimetry, nuclear magnetic resonance (1H-NMR and 13C-) spectroscopy, and HPLC-UV. The quantitative proton NMR results indicate that the sample is >95% CBD and the HPLC results indicate that 12 other commonly found cannabinoids (including THC) were less than the limit of detection of 0.004%.

Generation of FRET Biosensor cell lines

Stable transgenic biosensor-expressing cell lines were made in HaCaT and SK-N-BE(2) cells as previously described (Chapnick et al., 2015). Briefly, biosensor gene-containing plasmids were obtained through the addgene plasmid depository, and subcloned into our Bsr2 parent plasmid (sequence available upon request). Each biosensor Bsr2 plasmid was co-transfected with a PB recombinase expressing vector (mPB) via polymer based transfection using polyethyleneimine (PEI) (Polysciences, 25kD Linear).

Each stable transgenic cell line was selected for 7 days using 10 µg/ml Blasticidin S. FRET biosensor profiling was conducted in multiplexed parallel live cell experiments using 384 well imaging plates (Corning #3985) in an ImageXpress MicroXL high throughput microscope. Filters used for FRET measurements were the following: FRET excitation 438/24-25, dichroic 520LP, emission 542/27-25 (Semrock MOLE-0189); CFP excitation 438/24-25, dichroic 458LP, emission 483/32-25 (Semrock CFP-2432B-NTE-Zero). Time lapse microscopy images were collected, and FRET Ratio calculations for each site in each well at each time were performed as the mean value from pixels above threshold of background and flatfield corrected images, where each pixel value represented the FRET channel intensity divided by the CFP channel intensity. This method is described in more detail in our previous studies (Chapnick and Liu, 2014; Chapnick et al., 2015). Calculation and data visualization was performed in MATLAB using custom scripts that are available upon request.

EC50 estimation from FRET sensor dose responses

Dose responses at each time point were fit with the following fit function y = 1 / (1 + np.exp(-k*(x-EC50))) using python's scipy.optimize.curve_fit package. Prior to fitting, measurements were scaled between zero and one. R^2 goodness of fit was calculated between the sigmoid fit and the median of the replicates (duplicates) for each sensor/timepoint combination. Fits with EC_{50} estimates outside the dose range were discarded. EC_{50} values were kept for fits that resulted in a R^2 GOF > 0.75. The resulting distribution of EC_{50} values was somewhat bimodal resulting in a median EC_{50} of 8.48 µM across all sensors and times.

Transcriptomics Workflow:

CBD, and vehicle treatments were prepared in quadruplicate (4 drug treated/ 4 vehicle controls) at 3, 6, 12, and 24 hour timepoints. 500ng of Total RNA was used in Illumina TruSEQ mRNA library prep protocol. Libraries were run on the Illumina HiSEQ4000 at single read 150 bp length. Sequencing was performed on seven consecutive lanes. Median read counts per lane were ~49,000 with a CV of ~7%. Starting with 228 fastq files, each lane set was concatenated per condition. Run specifications were, 51 bp reads, standard single-read, first-stranded. Alignment to the human genome (HG19), was done using Tophat version 2.0.13. Two mismatches were allowed, and duplicate mapping was permitted at up to two locations. Using Trimmomatic-0.36, base pairs were trimmed if they dropped below a PHRED score of 15 within a sliding window of 4bp. Remaining reads shorter than 35 base pairs were removed. Illumina adapter sequences were also clipped using Trimmomatic. Fastqc was used to verify data integrity before and after trimming. Cufflinks/Cuffdiff 2.2.1 was used to obtain FPKM normalized gene count and differential expression measurements at each time point (Trapnell et al., 2010). One p/q-value was generated for each gene at each timepoint. Genes with a q-value significance < 0.05, and absolute $\log_2$ fold change of 1 or greater, for at least one time point, were retained for downstream analysis.

Proteomics Bioinformatics Workflow:

Protein quantification for time-series was performed with a Tandem Mass Tag (TMT) isobarically labeled 11-plex multiplexing scheme. The 15-point time series for each

cellular fraction was split into three series, with every series containing 5 treatment and matched control time point pairs, with 0 sec, 40 min, 3 hr, 12 hr, and 24 hr time points in Series A; 10 min, 80 min, 6 hr, 15 hr, and 48 hr in Series B; and 20 min, 2 hr, 9 hr, 18 hr, and 72 hr time points in Series C. This separation was performed so that a protein could be missing from one and/or two series due to stochastic effects in data-dependent acquisition and the overall trend could still be inferred, though with reduced resolution. The 11th label in each series was devoted to a global mix reference channel, which would be present in all series for a given cellular fraction. The global mix is a cell-fraction specific mixture that contains an equal portion from each time point sample. This channel was the denominator in the intermediate ratiometric measurement for differential expression for both drug-treated samples and time-matched controls. This mixture channel was constructed so that every measurable protein observed at any time point has a non-zero denominator when ratios are taken. When the differential expression is compared between the drug-treated labeled samples and matched control samples and expressed as a $\log_2$ ratio, the global mix reference channel cancels out.

The differential expression of each individual protein was determined using Bayesian methods for isobaric labeled proteomics data (Jow et al., 2014). Briefly, all observed peptides are mapped to a list of observed protein ID's via Isoform Resolver (Meyer-Arendt et al., 2011). The TMT 11-plex reporter ion spectrum peaks for each peptide contributes to the inference of the differential expression of a protein and reporter ion label. In this case, each reporter ion label represents a particular measured time point. The label-to-label normalization is handled via a hierarchical model, which calculates the bias inherent with each specific label by pooling differential expression estimates from all proteins, changing and unchanging. The hierarchical models are solved computationally with a Markov Chain Monte Carlo (MCMC) method, running chains in parallel for faster results (Denwood, 2016). The MCMC returns a Gaussian posterior probability distribution of $\log_2$ differential expression for each protein for each label. The model initially fits the ratiometric differential expression for every treatment and matched control relative to a global mix channel, and the reported drug-induced differential expression is the difference (in $\log_2$ space) between the treated sample and the matched control sample. Five MCMC chains were run independently for at least 500k steps, and convergences for each run were verified via Gelman-Rubin convergence variable < 1.05 (Gelman and Rubin, 1992).

The differential expression was calculated independently for all biological replicates so protein-level variance from separate replicates could be examined and quantified in the posterior distributions obtained from MCMC. For reporting a single differential expression for a protein and label, the Bayesian updating procedure is used to produce a single posterior distribution, from which a mean point estimate and 95% credible interval are calculated. In some specific instances, labels represent technical rather than biological replicates. In cases of technical replicates, the point estimate values were averaged and the credible intervals extents were treated as errors and added in quadrature. With this procedure, technical replicates contribute a single probability distribution to any further Bayesian updating.

For every cellular fraction and time point, then, there are between 3 and 6 biological replicates, and the number of replicates represented in the drug treated samples and

the matched control samples are not necessarily the same. The effect size (Cohen's *d*) was calculated between the posterior probability distributions of the drug treated and matched control samples as a standardized measure to determine if there was a drug effect. Statistical power analysis was performed to show that, with significance criteria $\alpha = 0.05$ and the statistical power requirement $(1-\beta) = 0.8$, the appropriate effect size threshold should be $d >$ (1.50, 1.75, 2.25, 3.38) for proteins observed within 6, 5, 4, or 3 replicates, respectively. A protein was selected for further consideration if it showed differential expression greater than this threshold for any given time point.

The Bioconductor Edge package (Leek et al., 2006) (DOI:10.18129/B9.bioc.edge) version 2.8.0 was used for time course differential analysis. Many proteins were not present for all replicates and/or plexes, so Edge was run sequentially to generate *p*-values for each case. For instance, in the soluble fraction, there were 273 proteins that were only present in two replicates. These were run through Edge separately from the other 1957 proteins that were observed in three replicates. The resulting time series *p*-values were combined into a list and FDR corrected using Benjamini-Hochberg multiple hypothesis correction (Benjamini and Hochberg, 1995).

Proteomics Network Analysis

Of the significantly changing proteins, correlation networks were generated for each subcellular fraction. Networks were created from the ethanol (vehicle) treated samples, as well as for the CBD treated samples. Network edge values were assigned using Spearman correlation coefficients between all proteins (vertices) for a given replicate. For each pair of proteins, 2*N edge values were generated, where N is the number of available replicate measurements for that protein. An independent *t*-test was used between basal replicate edge values and treatment edge values to evaluate what edges were significantly changed due to CBD treatment. Edges with $-\log_{10}(p\text{-value}) > 2$ ($p < 1\%$) were retained. Python graph-tool package was used to generate a stochastic block-model representation of the resulting network, which clusters nodes based on network connectivity similarity.

Combined Heatmap Criteria: All protein IDs with edge adjusted p-values less than 1% were merged with gene IDs from RNAseq with edge adjusted p-value < 1% and minimum absolute log2 fold change > 0.5. Merged list was used as input for Enrichr (Kuleshov et al., 2016) to get a table of GO terms (go_biological_processes_2017). GO terms were reduced using REVIGO with "medium" size setting: Terms with dispensability score less than 0.1 and q-value < 5% were kept. Merged IDs from remaining GO ontologies were clustered and plotted in heatmap by relative expression in CBD treated condition compared to vehicle control at each time point starting at 3 hours.

Subcellular Fractionation in Proteomics

For each sample, a 10 cm Petri Dish containing 10^6 SK-N-BE(2) cells was harvested and washed three times with 10 ml of 20°C PBS. All PBS was removed by aspiration and plates were frozen using liquid nitrogen and stored at -80°C overnight. Each plate was thawed on ice and 400 µl Tween20 Buffer (1x PBS, 0.1 % Tween20, 5 mM EDTA, 30 mM NaF, 1 mM NaVo4, 100 µM Leupeptin, 2.5 µM Pepstatin A) and scraped

thoroughly using a standard cell scraper. The resulting lysate was homogenized with a 200 µl pipette and transferred to 1.7 mL Eppendorf tube on ice. Lysate tubes were incubated for 30 min at 4°C rotating end-over-end. After rotation, tubes were centrifuged for 10 min at 4°C (16,100 rcf). All supernatant was transferred into new labeled 1.7mL Eppendorf. This tube contains insoluble buoyant plasma membrane and cytosol. The leftover pellet is the 'Membrane' fraction and is enriched in nuclei. 40µL of 1 M NaOAc was added to the supernatants, which immediately were exposed to centrifugation for 10 min at 4°C (16,100 rcf). All supernatant was transferred into new labeled 1.7mL Eppendorf. This is the 'Soluble' fraction. The pellet was resuspended in 400 µl 20 °C SDS buffer. This is 'Insoluble #2' fraction. All fraction containing tubes were filled completely with -20 °C Acetone and stored overnight in -20 °C. Each tube was exposed to centrifugation for 10 min at 4°C (16,100 rcf) and supernatants were aspirated and discarded, while pellets were allowed pellets to air dry 10 min 20 °C. The pellets then proceeded to the FASP procedure.

Quantitative Subcellular Proteomics

Sample preparation

Precipitated and dried subcellular protein extracts were solubilized with 4% (w/v) sodium dodecyl sulfate (SDS), 10mM Tris(2-carboxyethyl)phosphine (TCEP), 40mM chloroacetamide with 100mM Tris base pH 8.5. SDS lysates were boiled at 95°C for 10 minutes and then 10 cycles in a Bioruptor Pico (Diagenode) of 30 seconds on and 30 second off per cycle, or until protein pellets were completely dissolved. Samples were then cleared at 21,130 x g for 10 minutes at 20^0C, then digested into tryptic peptides using the filter-aided sample preparation (FASP) method (Wiśniewski, 2016). Briefly, SDS lysate samples were diluted 10-fold with 8M Urea, 0.1M Tris pH8.5 and loaded onto an Amicon Ultra 0.5mL 30kD NMWL cutoff (Millipore) ultrafiltration device. Samples were washed in the filters three time with 8M Urea, 0.1M Tris pH8.5, and again three times with 0.1M Tris pH8.5. Endoproteinase Lys-C (Wako) was added and incubated 2 hours rocking at room temperature, followed by trypsin (Pierce) which was incubated overnight rocking at room temperature. Tryptic peptides were eluted via centrifugation for 10 minutes at 10,000 x g, and desalted using an Oasis HLB cartridge (Waters) according to the manufacture instructions.

High pH C18 fractionation of TMT labeled peptides

Dried 10-plexed samples were then suspended in 20uL 3% (v/v) acetonitrile (ACN) and 0.1% (v/v) trifluoroacetic acid (TFA) and loaded onto a custom fabricated reverse phase C18 column (0.5 x 200mm C18, 1.8um 120Å Uchrom (nanoLCMS Solutions) maintained at 25^0 C and running 15uL/min with buffer A, 10mM ammonium formate, pH 10 and buffer B, 10mM ammonium formate, pH10 in 80% (v/v) ACN with a Waters M-class UPLC (Waters). Peptides were separated by gradient elution from 3% B to 50% B in 25 minutes, then from 50% B to 100% B in 5 minutes. Fractions were collected in seven rounds of concatenation for 30 s per fraction, then combined for a final of six high pH C18 fractions. Samples were dried and stored at -80^0 C until ready for LC/MS analyses.

Liquid Chromatography/Mass spectrometry analysis

Samples were suspended in 3% (v/v) acetonitrile, 0.1% (v/v) trifluoroacetic acid and direct injected onto a 1.7um, 130Å C18, 75um X 250mm M-class column (Waters), with a Waters M-class UPLC or a nanoLC1000 (Thermo Scientific). Tryptic peptides were gradient-eluted at 300nL/minute, from 3% acetonitrile to 20% acetonitrile in 100 minutes into an Orbitrap Fusion mass spectrometer (Thermo Scientific). Precursor mass spectrums (MS1) were acquired at 120,000 resolution from 380-1500 m/z with an automatic gain control (AGC) target of 2.0E5 and a maximum injection time of 50ms. Dynamics exclusion was set for 15 seconds with a mass tolerance of +/- 10 ppm. Quadrupole isolation for MS2 scans was 1.6 Da sequencing the most intense ions using Top Speed for a 3 second cycle time. All MS2 sequencing was performed using collision induced dissociation (CID) at 35% collision energy and scanned in the linear ion trap. An AGC target of 1.0E4 and 35 second maximum injection time was used. Selected-precursor selections of MS2 scans was used to isolate the five most intense MS2 fragment ions per scan to fragment at 65% collision energy using higher energy collision dissociation (HCD) with liberated TMT reporter ions scanned in the orbitrap at 60,000 resolution (FWHM). An AGC target of 1.0E5 and 240 second maximum injection time was used for all MS3 scans. All raw files were converted to mzML files and searched against the Uniprot Human database downloaded April 1, 2015 using Mascot v2.5 with cysteine carbamidomethylation as a fixed modification, methionine oxidation, and protein N-terminal acetylation were searched as variable modifications. Peptide mass tolerance was 20ppm for MS1 and 0.5mDa for MS2. All peptides were thresholded at a 1% false discovery rate (FDR).

Phosphoproteomics

Sample preparation and phosphopeptide enrichment

SK-N-BE(2) cells were cultured in SILAC media either with Lys8 and Arg10 (Heavy) or Lys0 and Arg0 (Light). Two biological replicates of near confluent Heavy cells and two replicates of near confluent Light cells were treated with 20uM CBD for 10 minutes (4 replicates), 1 hour (4 replicates) and 3 hours (4 replicates) for phosphoproteomics analysis. Cells were harvested in 4% (w/v) SDS, 100mM Tris, pH 8.5 and boiled at 95^0 C for 5 minutes. Samples were reduced with 10mM TCEP and alkylated with 50mM chloroacetamide, then digested using the FASP protocol, with the following modifications: an Amicon Ultra 0.5mL 10kD NMWL cutoff (Millipore) ultrafiltration device was used rather than a 30kD NMWL cutoff. Tryptic peptides were cleaned a Water HLB Oasis cartridge (Waters) and eluted with 65% (v/v) ACN, 1% TFA. Glutamic acid was added to 140mM and TiO2 (Titanshere, GL Sciences) was added at a ratio of 10mg TiO:1 mg tryptic peptides and incubated for 15 minutes at ambient. The phosphopeptide-bound TiO2 beads were washed with 65% (v/v) ACN, 0.5% TFA and again with 65% (v/v) ACN, 0.1% TFA, then transferred to a 200uL C8 Stage Tip (Thermo Scientific). Phosphopeptides were eluted with 65% (v/v) ACN, 1% (v/v) ammonium hydroxide and lyophilized dry.

High pH C18 fractionation of enriched phosphopeptides

Enriched phosphopeptide samples were then suspended in 20uL 3% (v/v) acetonitrile (ACN) and 0.1% (v/v) trifluoroacetic acid (TFA) and loaded onto a custom fabricated reverse phase C18 column (0.5 x 200mm C18, 1.8um 120Å Uchrom (nanoLCMS

Solutions) maintained at 25^0 C and running 15uL/min with buffer A, 10mM ammonium formate, pH 10 and buffer B, 10mM ammonium formate, pH10 in 80% (v/v) ACN with a Waters M-class UPLC (Waters). Peptides were separated by gradient elution from 3% B to 50% B in 25 minutes, then from 50% B to 100% B in 5 minutes. Fractions were collected in seven rounds of concatenation for 30 sec per fraction for a final of twelve high pH C18 fractions. Samples were dried and stored at -80^0 C until analysis.

Liquid Chromatography/Mass spectrometry analysis of phosphopeptide fractions

Samples were suspended in 3% (v/v) acetonitrile, 0.1% (v/v) trifluoroacetic acid and direct injected onto a 1.7um, 130Å C18, 75um X 250mm M-class column (Waters), with a Waters M-class UPLC. Tryptic peptides were gradient eluted at 300nL/minute, from 3% acetonitrile to 20% acetonitrile in 100 minutes into an Orbitrap Fusion mass spectrometer (Thermo Scientific). Precursor mass spectrums (MS1) were acquired at 120,000 resolution from 380-1500 m/z with an AGC target of 2.0E5 and a maximum injection time of 50ms. Dynamics exclusion was set for 20 seconds with a mass tolerance of +/- 10 ppm. Isolation for MS2 scans was 1.6 Da using the quadrupole, and the most intense ions were sequenced using Top Speed for a 3 second cycle time. All MS2 sequencing was performed using higher energy collision dissociation (HCD) at 35% collision energy and scanned in the linear ion trap. An AGC target of 1.0E4 and 35 second maximum injection time was used. Rawfiles were searched against the Uniprot human database using Maxquant with cysteine carbamidomethylation as a fixed modification. Methionine oxidation, protein N-terminal acetylation, and phosphorylation of serine, threonine and tyrosine were searched as variable modifications. All peptides and proteins were thresholded at a 1% false discovery rate (FDR).

Bulk Metabolomics Sample Preparation

Cultured cells were harvested, washed with PBS, flash frozen, and stored at -80C until analysis. Prior to LC-MS analysis, samples were placed on ice and re-suspended with methanol:acetonitrile:water (5:3:2, v/v/v) at a concentration of 2 million cells per ml. Suspensions were vortexed continuously for 30 min at 4°C. Insoluble material was removed by centrifugation at 10,000 g for 10 min at 4°C and supernatants were isolated for metabolomics analysis by UHPLC-MS. This method was used for cholesterol precursors and free headgroups.

UHPLC-MS analysis for Bulk Metabolomics

Analyses were performed as previously published (Nemkov et al., 2017, 2019). Briefly, the analytical platform employs a Vanquish UHPLC system (Thermo Fisher Scientific, San Jose, CA, USA) coupled online to a Q Exactive mass spectrometer (Thermo Fisher Scientific, San Jose, CA, USA). Samples were resolved over a Kinetex C18 column, 2.1 x 150 mm, 1.7 µm particle size (Phenomenex, Torrance, CA, USA) equipped with a guard column (SecurityGuard™ Ultracartridge – UHPLC C18 for 2.1 mm ID Columns – AJO-8782 – Phenomenex, Torrance, CA, USA) (A) of water and 0.1% formic acid and a mobile phase (B) of acetonitrile and 0.1% formic acid for positive ion polarity mode, and an aqueous phase (A) of water:acetonitrile (95:5) with 1 mM ammonium acetate and a mobile phase (B) of acetonitrile:water (95:5) with 1 mM ammonium acetate for negative ion polarity mode. Samples were eluted from the column using either an isocratic elution

of 5% B flowed at 250 µl/min and 25ºC or a gradient from 5% to 95% B over 1 minute, followed by an isocratic hold at 95% B for 2 minutes, flowed at 400 µl/min and 30ºC. The Q Exactive mass spectrometer (Thermo Fisher Scientific, San Jose, CA, USA) was operated independently in positive or negative ion mode, scanning in Full MS mode (2 µscans) from 60 to 900 m/z at 70,000 resolution, with 4 kV spray voltage, 15 sheath gas, 5 auxiliary gas. Calibration was performed prior to analysis using the Pierce™ Positive and Negative Ion Calibration Solutions (Thermo Fisher Scientific). Acquired data was then converted from raw to .mzXML file format using Mass Matrix (Cleveland, OH, USA). Metabolite assignments, isotopologue distributions, and correction for expected natural abundances of deuterium, ^{13}C, and ^{15}N isotopes were performed using MAVEN (Princeton, NJ, USA).(Clasquin et al., 2012) Graphs, heat maps and statistical analyses (either T-Test or ANOVA), metabolic pathway analysis, PLS-DA and hierarchical clustering was performed using the MetaboAnalyst package (www.metaboanalyst.com)(Chong et al., 2018).

Lipidomics Sample Preparation

Extraction of cholesterol, precursors, free fatty acids, cholesteryl esters, and phospho lipids were performed in the following manner. SK-N-BE(2) cells in 10 cm dishes were washed with 10 mL PBS twice and then cells were scraped and pelleted at 400 rcf for 2 minutes. Cell pellets were resuspended in 100% methanol at 4°C and sonicate at 70% power in 10 pulses, 5 seconds on/5 seconds off. The resulting lysate was rotated for 60 minutes at room temperature, followed by centrifugation for 20 min at 4°C (16,100 rcf). Subcellular fractionation of organelles from intact SK-N-BE(2) cells was done in the following manner to assess subcellular CBD distribution. Cells in 10 cm culture dishes were harvest by washing twice with 10 mL PBS at room temperature, followed by trypsinization using a cell culture grade Trypsin/EDTA solution (ThermoFisher). Trypsinized cells were quenched by addition of 2 mL 10% FBS containing DMEM and cells were pelleted by centrifugation for 2 min at 4°C (200 rcf). Cell pellets were wash one time with 10 mL PBS, and resuspended in 1 mL Tween20 Buffer (1x PBS, 0.05 % Tween20, 5 mM EDTA). This lysate was subjected to mechanical disruption using a 1mL glass Dounce homogenizer, 10 full passes at 4°C. Nuclei was pelleted from homogenate by centrifugation for 5 min at 4°C (2,000 rcf). Supernatant was separated and insoluble ER membranes were pelleted by centrifugation for 10 min at 4°C (4,000 rcf). Supernatant was separated and insoluble plasma membranes were pelleted by centrifugation for 10 min at 4°C (16,000 rcf). Extraction of all fractions was done in 100% methanol for 2 hours at room temperature and rotation end-over-end, followed by removal of insoluble material by centrifugation for 20 min at 20°C (16,100 rcf).

UHPLC-MS analysis for Lipidomics

Samples were analyzed as published (Reisz et al., 2019). Briefly, analytes were resolved over an ACQUITY HSS T3 column (2.1 x 150 mm, 1.8 µm particle size (Waters, MA, USA) using an aqueous phase (A) of 25% acetonitrile and 5 mM ammonium acetate and a mobile phase (B) of 90% isopropanol, 10% acetonitrile and 5 mM ammonium acetate. The column was equilibrated at 30% B, and upon injection of 10 µL of extract, samples were eluted from the column using the solvent gradient: 0-9 min 30-100% B and 0.325 mL/min; hold at 100% B for 3 min at 0.3 mL/min, and then

decrease to 30% over 0.5 min at 0.4 ml/min, followed by a re-equilibration hold at 30% B for 2.5 minutes at 0.4 ml/min. The Q-Exactive mass spectrometer (Thermo Fisher) was operated in positive and negative ion mode using electrospray ionization, scanning in Full MS mode (2 µscans) from 150 to 1500 m/z at 70,000 resolution, with 4 kV spray voltage, 45 shealth gas, 15 auxiliary gas. When required, dd-MS2 was performed at 17,500 resolution, AGC target = 1e5, maximum IT = 50 ms, and stepped NCE of 25, 35 for positive mode, and 20, 24, and 28 for negative mode. Calibration was performed prior to analysis using the PierceTM Positive and Negative Ion Calibration Solutions (Thermo Fisher). Acquired data was then converted from .raw to .mzXML file format using Mass Matrix (Cleveland, OH, USA). Samples were analyzed in randomized order with a technical mixture injected incrementally to qualify instrument performance. This technical mixture was also injected three times per polarity mode and analyzed with the parameters above, except CID fragmentation was included for unknown compound identification. Metabolite assignments were made based on accurate intact mass (sub 5 ppm), isotope distributions, and relative retention times, and comparison to analytical standards in the SPLASH Lipidomix Mass Spec Standard (Avanti Polar Lipids) using MAVEN (Princeton, NJ, USA). Discovery mode analysis was performed with standard workflows using Compound Discoverer and Lipid Search 4.0 (Thermo Fisher Scientific, San Jose, CA).

Confocal Microscopy of Cholesterol and Lysosomes

SK-N-BE(2) cells were seeded into fibronectin coated glass bottom 96 well plates (Matriplate) at a cell density of 40,000 cells/well using low background imaging media (FluoroBrite DMEM with all supplements described, above). At the time of seeding, lysotracker Deep Red (ThermoFisher) was added at a 1000x dilution and NBD-cholesterol (ThermoFisher) was added at a final concentration of 10 µg/mL. After 24 hrs, CBD or ethanol vehicle was added to a final concentration of 20 µM and incubated for an additional 24 hrs prior to imaging using a Nikon A1R laser scanning confocal microscope for acquisition with the FITC and TRITC channels. In experiments using U18666A, a final concentration of 10 µg/ml was used and was added simultaneously with CBD.

Assaying Cell Viability and Apoptosis

Cell viability for SK-N-BE(2) cells was conducted using a fluorometric cell viability assay using Resazurin (PromoKine) according to the manufacturer's instructions. Measurement of percent apoptotic cells was done in 384 well imaging plates (Corning #3985) seeded with 2,000 cells/well and stained with Hoescht 33258 (1µg/mL) and CellEvent Caspase-3/7 Green Detection Reagent (ThermoFisher) at a dilution of 1000x. Dyes were added at the time of seeding, 18-24 hours prior to performing experiments. For experiments using atorvastatin, atorvastatin was added 24 hrs prior to addition of CBD. For experiments involving 25-hydroxy cholesterol, U18666A, and VULM 1457, inhibitors were added simultaneously with CBD. Experiments were performed using an ImageXpress MicroXL microscope and a 10x objective, where images were acquired for each well at the indicated time-points using DAPI and FITC filter sets. Using MATLAB, images were processed with custom written scripts (available upon request) that

perform flatfield & background correction, identification of all cells (DAPI channel) using standard threshold above background techniques, and identification of apoptotic cells using a similar method in the FITC channel. Percent apoptotic cells was calculated from the sum of apoptotic cell pixels divided by the sum of all cell pixels for each field of view. Error displayed is the standard deviation from between 2 and 4 biological replicates.

Fluorometric Cholesterol Oxidase Experiments and SUV preparation

SUVs were prepared by dissolving 10 mg L-α-Phosphatidylcholine (Sigma P3556) in 100 µL chloroform in a glass vial, followed by removal of solvent under vacuum at room temperature for 1 hour. For experiments using cholesterol containing SUVs, 0.74 mg of cholesterol (Sigma C8667) was mixed with 10 mg L-α-Phosphatidylcholine prior to removal of chloroform solvent. Following solvent removal, 100 µL PBS was added and a microtip sonicator was inserted to perform sonication at 70% power, 10 pulses, 5 seconds on/off at room temperature. SUVs in suspension were brought to a volume of 1 mL with addition of PBS. The resulting SUVs in suspension were used at a dilution of 100-fold in subsequent cholesterol oxidase reactions. Cholesterol oxidase reactions were performed using reagents from the Amplex Red Cholesterol Assay Kit (ThermoFisher A12216), where each reaction was performed in 50 µL volumes using: 0.5 µL SUVs solution, 0.05 µL cholesterol oxidase solution, 0.05 µL HRP solution, 0.05 µL Amplex Red/DMSO made according to manufacturer's instructions, and the indicated CBD concentrations in PBS. Reaction volume was brought to 50 µL using PBS. In cases where SUVs were not used, either 1 µg/reaction 25-OH cholesterol or 5 µg/reaction MBCD:Cholesterol (1:2) was substituted for SUVs. MBCD:Cholesterol was prepared as previously described (Widenmaier et al., 2017). Cholesterol oxidase reactions were performed in Corning 384 well optical imaging plates (#3985) in an ImageXpress MicroXL widefield fluorescence microscope using the TRITC filter sets, where 1 ms exposure time images were taken of each well 20 µm above the well bottom every 10 minutes for 5 hours at 37 °C, using a 10x objective. Images were flatfield corrected and the sum of fluorescence intensity across all 540x540 pixels was calculated using custom MATLAB scripts that are available upon request. Product formation of Amplex red was found to be linear within 0-1 hours, and data between t=0 and t=1 hours was used to calculate the average rate of increase in TRITC fluorescence using Microsoft Excel. Displayed error bars represent the standard deviation of three or more replicate reactions.

FRAP Experiments Using Synthetic Membranes

The formulation and techniques to create SUVs were repeated with addition of 108 µg of 22-NBD cholesterol to L-α-Phosphatidylcholine and cholesterol prior to the solvent removal step described for preparation of SUVs. A 1:5 dilution of NBD-cholesterol containing SUV suspension:PBS was added to each well of glass bottom 96 well plates (MatriPlate MGB096-1-2-LG-L) such that each well contains 100 µl of diluted SUV suspension. 96 well plates were exposed to centrifugation for 20 minutes at 2000 rcf using a swinging bucket rotor at room temperature. A microtip sonicator was inserted into each well to perform sonication at 20% power, 20 pulses, 2 seconds on/off at room temperature. The contents of each well was washed three times with 150 µl of PBS, and subsequent experiments were performed with 250 µl PBS containing ethanol vehicle, 20

μM CBD and/or 20 μM DHA. CBD and DHA were incubated in wells for 1 hr at room temperature prior to imaging and FRAP experiments using a Nikon A1R microscope. Photobleaching was performed using Nikon Elements software with the following parameters: framerate 250 ms, 100% power 488 laser for photobleaching for 250 ms, and optical settings for FITC. Analysis was performed using ImageJ and Microsoft Excel. All trends were normalized by division of mean intensity within the photobleached region to a region of identical size remote from the photobleached region. Error bars indicate the standard error of the mean from three replicates.

Seahorse Extracellular Flux Analysis

Oxygen consumption rate and extracellular acidification rate were measured using the SeahorseXF^{e}24 Extracellular Flux Analyzer and the Agilent Seahorse XF Cell Energy Phenotype Test Kit. Cells were plated at 2x10^4 cells per well in XF^{e}24 microplates. Cells were treated with either 20 μM CBD or ethanol as a vehicle control either 24 hours or 2 hours prior to assaying. The day of the assay cells were washed with an assay medium containing 20 μM CBD or vehicle and placed at 37°C in a CO2 free incubator for 1 hour. 1 μM Oligomycin and 1 μM FCCP were injected by the Seahorse analyzer as oxygen consumption rate and extracellular acidification rate were measured per manufacturer's protocol.

Resource Availability

All unique/stable reagents generated in this study are available from the lead contact, William Old (william.old@colorado.edu) with a completed Materials Transfer Agreement.

Data and Code Availability Statements

Proteomics and phosphoproteomics raw data is available at the MassiVE repository ID MSV000085479 accessible at https://doi.org/doi:10.25345/C5571V

Source data for RNAseq experiments is accessible at GEO with the identifier GSE151512 at https://www.ncbi.nlm.nih.gov/geo/query/acc.cgi?acc=GSE151512

The code generated during this study is available at GitHub, DOI:10.5281/zenodo.3861043, URL: https://github.com/CUOldLab/cbd-manuscript-code-guardse-2020

Supplemental Tables Summary

Table S1. Global Metabolomics Results, Related to Figure 1C and Supplementary Figures Throughout

Table S2. Phosphoproteome Results, Related to Figure 2

Table S3. Cytosolic Proteome Results, Related to Figure 3

Table S4. Nuclear Proteome Results, Related to Figure 3

Table S5. Membrane Proteome Results, Related to Figure 3

Table S6. RNAseq Differential Analysis Results, Related to Figure 3D

Table S7. Lipidomics Results, Related to Figure 4

References

Ahn, K., and Sampson, N.S. (2004). Cholesterol Oxidase Senses Subtle Changes in Lipid Bilayer Structure. Biochemistry *43*, 827–836.

Ahrens, J., Demir, R., Leuwer, M., de la Roche, J., Krampfl, K., Foadi, N., Karst, M., and Haeseler, G. (2009). The nonpsychotropic cannabinoid cannabidiol modulates and directly activates alpha-1 and alpha-1-Beta glycine receptor function. Pharmacology *83*, 217–222.

Alharris, E., Singh, N.P., Nagarkatti, P.S., Nagarkatti, M., Alharris, E., Singh, N.P., Nagarkatti, P.S., and Nagarkatti, M. (2019). Role of miRNA in the regulation of cannabidiol-mediated apoptosis in neuroblastoma cells. Oncotarget *10*, 45–59.

Amsalem, M., Poilbout, C., Ferracci, G., Delmas, P., and Padilla, F. (2018). Membrane cholesterol depletion as a trigger of Nav1.9 channel-mediated inflammatory pain. EMBO J *37*.

Bang, B., Gniadecki, R., and Gajkowska, B. (2005). Disruption of lipid rafts causes apoptotic cell death in HaCaT keratinocytes. Exp. Dermatol. *14*, 266–272.

Benjamini, Y., and Hochberg, Y. (1995). Controlling the False Discovery Rate: A Practical and Powerful Approach to Multiple Testing. Journal of the Royal Statistical Society: Series B (Methodological) *57*, 289–300.

Berger, L., Slein, M.W., Colowick, S.P., and Cori, C.F. (1946). ISOLATION OF HEXOKINASE FROM BAKER'S YEAST. J. Gen. Physiol. *29*, 379–391.

Besprozvannaya, M., Dickson, E., Li, H., Ginburg, K.S., Bers, D.M., Auwerx, J., and Nunnari, J. (2018). GRAM domain proteins specialize functionally distinct ER-PM contact sites in human cells. ELife *7*, e31019.

Bisogno, T., Hanuš, L., De Petrocellis, L., Tchilibon, S., Ponde, D.E., Brandi, I., Moriello, A.S., Davis, J.B., Mechoulam, R., and Di Marzo, V. (2001). Molecular targets for cannabidiol and its synthetic analogues: Effect on vanilloid VR1 receptors and on the cellular uptake and enzymatic hydrolysis of anandamide. British Journal of Pharmacology *134*, 845–852.

Blais, J.D., Filipenko, V., Bi, M., Harding, H.P., Ron, D., Koumenis, C., Wouters, B.G., and Bell, J.C. (2004). Activating transcription factor 4 is translationally regulated by hypoxic stress. Mol. Cell. Biol. *24*, 7469–7482.

Blum, B.C., Mousavi, F., and Emili, A. (2018). Single-platform 'multi-omic' profiling: unified mass spectrometry and computational workflows for integrative proteomics–metabolomics analysis. Mol. Omics *14*, 307–319.

Brown, M.S., and Goldstein, J.L. (1997). The SREBP pathway: regulation of cholesterol metabolism by proteolysis of a membrane-bound transcription factor. Cell *89*, 331–340.

Brown, M.S., Ho, Y.K., and Goldstein, J.L. (1980). The cholesteryl ester cycle in macrophage foam cells. Continual hydrolysis and re-esterification of cytoplasmic cholesteryl esters. J. Biol. Chem. *255*, 9344–9352.

Carlson, C.A., and Kim, K.-H. (1973). Regulation of Hepatic Acetyl Coenzyme A Carboxylase by Phosphorylation and Dephosphorylation. J. Biol. Chem. *248*, 378–380.

Chang, T.-Y., Reid, P.C., Sugii, S., Ohgami, N., Cruz, J.C., and Chang, C.C.Y. (2005). Niemann-Pick Type C Disease and Intracellular Cholesterol Trafficking. Journal of Biological Chemistry *280*, 20917–20920.

Chang, T.Y., Li, B.L., Chang, C.C.Y., and Urano, Y. (2009). Acyl-coenzyme A:cholesterol acyltransferases.

Chapnick, D.A., and Liu, X. (2014). Leader cell positioning drives wound-directed collective migration in TGFβ-stimulated epithelial sheets. Molecular Biology of the Cell *25*, 1586–1593.

Chapnick, D.A., Bunker, E., and Liu, X. (2015). A biosensor for the activity of the "sheddase" TACE (ADAM17) reveals novel and cell type-specific mechanisms of TACE activation. Science Signaling *8*.

Chapnick, D.A., Bunker, E., Liu, X., and Old, W.M. (2019). Temporal Metabolite, Ion, and Enzyme Activity Profiling Using Fluorescence Microscopy and Genetically Encoded Biosensors. Methods Mol. Biol. *1978*, 343–353.

Cheng, D., Chang, C.C., Qu, X., and Chang, T.Y. (1995). Activation of acyl-coenzyme A:cholesterol acyltransferase by cholesterol or by oxysterol in a cell-free system. J. Biol. Chem. *270*, 685–695.

Chong, J., Soufan, O., Li, C., Caraus, I., Li, S., Bourque, G., Wishart, D.S., and Xia, J. (2018). MetaboAnalyst 4.0: Towards more transparent and integrative metabolomics analysis. Nucleic Acids Research *46*, W486–W494.

Clasquin, M.F., Melamud, E., and Rabinowitz, J.D. (2012). LC-MS data processing with MAVEN: A metabolomic analysis and visualization engine. Current Protocols in Bioinformatics.

Dale, S., Wilson, W.A., Edelman, A.M., and Hardie, D.G. (1995). Similar substrate recognition motifs for mammalian AMP-activated protein kinase, higher plant HMG-CoA

reductase kinase-A, yeast SNF1, and mammalian calmodulin-dependent protein kinase I. FEBS Letters *361*, 191–195.

Das, A., Brown, M.S., Anderson, D.D., Goldstein, J.L., and Radhakrishnan, A. (2014). Three pools of plasma membrane cholesterol and their relation to cholesterol homeostasis. Elife *3*.

Dasari, A., Bartholomew, J.N., Volonte, D., and Galbiati, F. (2006). Oxidative Stress Induces Premature Senescence by Stimulating Caveolin-1 Gene Transcription through p38 Mitogen-Activated Protein Kinase/Sp1–Mediated Activation of Two GC-Rich Promoter Elements. Cancer Res *66*, 10805–10814.

Davignon, J. (2004). Beneficial cardiovascular pleiotropic effects of statins. Circulation *109*, III39-43.

De Felice, B., Santillo, M., Serù, R., Damiano, S., Matrone, G., Wilson, R.R., and Mondola, P. (2004). Modulation of 3-hydroxy-3-methylglutaryl-CoA reductase gene expression by CuZn superoxide dismutase in human fibroblasts and HepG2 cells. Gene Expr. *12*, 29–38.

De Filippis, D., Esposito, G., Cirillo, C., Cipriano, M., De Winter, B.Y., Scuderi, C., Sarnelli, G., Cuomo, R., Steardo, L., De Man, J.G., et al. (2011). Cannabidiol reduces intestinal inflammation through the control of neuroimmune axis. PLoS ONE *6*, e28159.

Demais, V., Barthélémy, A., Perraut, M., Ungerer, N., Keime, C., Reibel, S., and Pfrieger, F.W. (2016). Reversal of Pathologic Lipid Accumulation in NPC1-Deficient Neurons by Drug-Promoted Release of LAMP1-Coated Lamellar Inclusions. J. Neurosci. *36*, 8012–8025.

Devinsky, O., Cross, J.H., Laux, L., Marsh, E., Miller, I., Nabbout, R., Scheffer, I.E., Thiele, E.A., and Wright, S. (2017). Trial of Cannabidiol for Drug-Resistant Seizures in the Dravet Syndrome (Massachusetts Medical Society).

Dravet, C. (2011). The core Dravet syndrome phenotype. Epilepsia *52 Suppl 2*, 3–9.

Esposito, G., Scuderi, C., Valenza, M., Togna, G.I., Latina, V., De Filippis, D., Cipriano, M., Carratù, M.R., Iuvone, T., and Steardo, L. (2011). Cannabidiol reduces Aβ-induced neuroinflammation and promotes hippocampal neurogenesis through PPARγ involvement. PLoS ONE *6*, e28668.

Fediuc, S., Gaidhu, M.P., and Ceddia, R.B. (2006). Regulation of AMP-activated protein kinase and acetyl-CoA carboxylase phosphorylation by palmitate in skeletal muscle cells. J. Lipid Res. *47*, 412–420.

Ferreri, C. (2005). Life—As a Matter of Fat: The Emerging Science of Lipidomics.By Ole G. Mouritsen. ChemBioChem *6*, 1463–1464.

Gaston, T.E., Bebin, E.M., Cutter, G.R., Liu, Y., Szaflarski, J.P., and UAB CBD Program (2017). Interactions between cannabidiol and commonly used antiepileptic drugs. Epilepsia *58*, 1586–1592.

Gelman, A., and Rubin, D.B. (1992). Inference from iterative simulation using multiple sequences. Statistical Science *7*, 457–472.

Geng, L., Zhou, W., Liu, B., Wang, X., and Chen, B. (2018). DHA induces apoptosis of human malignant breast cancer tissues by the TLR-4/PPAR-α pathways. Oncol Lett *15*, 2967–2977.

George, K.S., and Wu, S. (2012). Lipid raft: A floating island of death or survival. Toxicology and Applied Pharmacology *259*, 311–319.

Ghovanloo, M.-R., Shuart, N.G., Mezeyova, J., Dean, R.A., Ruben, P.C., and Goodchild, S.J. (2018). Inhibitory effects of cannabidiol on voltage-dependent sodium currents. J. Biol. Chem. *293*, 16546–16558.

Gianfrancesco, M.A., Paquot, N., Piette, J., and Legrand-Poels, S. (2018). Lipid bilayer stress in obesity-linked inflammatory and metabolic disorders. Biochem. Pharmacol. *153*, 168–183.

Giannini, E.G., Testa, R., and Savarino, V. (2005). Liver enzyme alteration: a guide for clinicians. CMAJ *172*, 367–379.

Gray, R.A., and Whalley, B.J. (2020). The proposed mechanism of action of CBD in epilepsy. Epileptic Disorders : International Epilepsy Journal with Videotape *22*, 10–15.

Gwinn, D.M., Shackelford, D.B., Egan, D.F., Mihaylova, M.M., Mery, A., Vasquez, D.S., Turk, B.E., and Shaw, R.J. (2008). AMPK Phosphorylation of Raptor Mediates a Metabolic Checkpoint. Molecular Cell *30*, 214–226.

Hafner, M., Mills, C.E., Subramanian, K., Chen, C., Chung, M., Boswell, S.A., Everley, R.A., Liu, C., Walmsley, C.S., Juric, D., et al. (2019). Multiomics Profiling Establishes the Polypharmacology of FDA-Approved CDK4/6 Inhibitors and the Potential for Differential Clinical Activity. Cell Chemical Biology *26*, 1067–1080.e8.

Hardie, D.G., Salt, I.P., Hawley, S.A., and Davies, S.P. (1999). AMP-activated protein kinase: an ultrasensitive system for monitoring cellular energy charge. Biochem. J. *338 (Pt 3)*, 717–722.

Hawley, S.A., Boudeau, J., Reid, J.L., Mustard, K.J., Udd, L., Mäkelä, T.P., Alessi, D.R., and Hardie, D.G. (2003). Complexes between the LKB1 tumor suppressor, STRAD alpha/beta and MO25 alpha/beta are upstream kinases in the AMP-activated protein kinase cascade. J. Biol. *2*, 28.

Hawley, S.A., Pan, D.A., Mustard, K.J., Ross, L., Bain, J., Edelman, A.M., Frenguelli, B.G., and Hardie, D.G. (2005). Calmodulin-dependent protein kinase kinase-β is an alternative upstream kinase for AMP-activated protein kinase. Cell Metabolism *2*, 9–19.

Hinz, B., and Ramer, R. (2019). Anti-tumour actions of cannabinoids. Br. J. Pharmacol. *176*, 1384–1394.

Höglinger, D., Burgoyne, T., Sanchez-Heras, E., Hartwig, P., Colaco, A., Newton, J., Futter, C.E., Spiegel, S., Platt, F.M., and Eden, E.R. (2019). NPC1 regulates ER contacts with endocytic organelles to mediate cholesterol egress. Nature Communications *10*, 4276.

Hsu, J.-L., Leu, W.-J., Hsu, L.-C., Liu, S.-P., Zhong, N.-S., and Guh, J.-H. (2018). Para-Toluenesulfonamide Induces Anti-tumor Activity Through Akt-Dependent and -Independent mTOR/p70S6K Pathway: Roles of Lipid Raft and Cholesterol Contents. Front Pharmacol *9*, 1223.

Ibeas Bih, C., Chen, T., Nunn, A.V.W., Bazelot, M., Dallas, M., and Whalley, B.J. (2015). Molecular Targets of Cannabidiol in Neurological Disorders. Neurotherapeutics *12*, 699–730.

Iffland, K., and Grotenhermen, F. (2017). An Update on Safety and Side Effects of Cannabidiol: A Review of Clinical Data and Relevant Animal Studies. Cannabis and Cannabinoid Research *2*, 139–154.

Jow, H., Boys, R.J., and Wilkinson, D.J. (2014). Bayesian identification of protein differential expression in multi-group isobaric labelled mass spectrometry data. Statistical Applications in Genetics and Molecular Biology *13*, 531–551.

Kenyon, J., Liu, W., and Dalgleish, A. (2018). Report of Objective Clinical Responses of Cancer Patients to Pharmaceutical-grade Synthetic Cannabidiol. Anticancer Res. *38*, 5831–5835.

Kilsdonk, E.P., Yancey, P.G., Stoudt, G.W., Bangerter, F.W., Johnson, W.J., Phillips, M.C., and Rothblat, G.H. (1995). Cellular cholesterol efflux mediated by cyclodextrins. J. Biol. Chem. *270*, 17250–17256.

Klein, U., Gimpl, G., and Fahrenholz, F. (1995). Alteration of the myometrial plasma membrane cholesterol content with beta-cyclodextrin modulates the binding affinity of the oxytocin receptor. Biochemistry *34*, 13784–13793.

Krämer, A., Green, J., Pollard, J., and Tugendreich, S. (2014). Causal analysis approaches in Ingenuity Pathway Analysis. Bioinformatics *30*, 523–530.

Kuleshov, M.V., Jones, M.R., Rouillard, A.D., Fernandez, N.F., Duan, Q., Wang, Z., Koplev, S., Jenkins, S.L., Jagodnik, K.M., Lachmann, A., et al. (2016). Enrichr: a comprehensive gene set enrichment analysis web server 2016 update. Nucleic Acids Res. *44*, W90-97.

Lange, Y., Ye, J., Rigney, M., and Steck, T.L. (1999). Regulation of endoplasmic reticulum cholesterol by plasma membrane cholesterol. J. Lipid Res. *40*, 2264–2270.

Lange, Y., Tabei, S.M.A., Ye, J., and Steck, T.L. (2013). Stability and Stoichiometry of Bilayer Phospholipid–Cholesterol Complexes: Relationship to Cellular Sterol Distribution and Homeostasis. Biochemistry *52*, 6950–6959.

Lauckner, J.E., Jensen, J.B., Chen, H.-Y., Lu, H.-C., Hille, B., and Mackie, K. (2008). GPR55 is a cannabinoid receptor that increases intracellular calcium and inhibits M current. Proc. Natl. Acad. Sci. U.S.A. *105*, 2699–2704.

Leek, J.T., Monsen, E., Dabney, A.R., and Storey, J.D. (2006). EDGE: extraction and analysis of differential gene expression. Bioinformatics *22*, 507–508.

Li, X., Wang, L., Zhou, X.E., Ke, J., de Waal, P.W., Gu, X., Tan, M.H.E., Wang, D., Wu, D., Xu, H.E., et al. (2015). Structural basis of AMPK regulation by adenine nucleotides and glycogen. Cell Research *25*, 50–66.

Lindblom, G., and Orädd, G. (2009). Lipid lateral diffusion and membrane heterogeneity. Biochim. Biophys. Acta *1788*, 234–244.

Lingwood, D., and Simons, K. (2010). Lipid rafts as a membrane-organizing principle. Science *327*, 46–50.

Liou, G.I., Auchampach, J.A., Hillard, C.J., Zhu, G., Yousufzai, B., Mian, S., Khan, S., and Khalifa, Y. (2008). Mediation of cannabidiol anti-inflammation in the retina by equilibrative nucleoside transporter and A2A adenosine receptor. Invest. Ophthalmol. Vis. Sci. *49*, 5526–5531.

Liu, M., Huang, W., Wu, D., and Priestley, J.V. (2006). TRPV1, but not P2X, requires cholesterol for its function and membrane expression in rat nociceptors. European Journal of Neuroscience *24*, 1–6.

Lu, F., Liang, Q., Abi-Mosleh, L., Das, A., De Brabander, J.K., Goldstein, J.L., and Brown, M.S. (2015). Identification of NPC1 as the target of U18666A, an inhibitor of lysosomal cholesterol export and Ebola infection. ELife *4*, e12177.

Lundbæk, J.A., Birn, P., Girshman, J., Hansen, A.J., and Andersen, O.S. (1996). Membrane Stiffness and Channel Function. Biochemistry *35*, 3825–3830.

Lundbaek, J.A., Birn, P., Tape, S.E., Toombes, G.E.S., Søgaard, R., Koeppe, R.E., Gruner, S.M., Hansen, A.J., and Andersen, O.S. (2005). Capsaicin regulates voltage-dependent sodium channels by altering lipid bilayer elasticity. Mol. Pharmacol. *68*, 680–689.

Massi, P., Solinas, M., Cinquina, V., and Parolaro, D. (2013). Cannabidiol as potential anticancer drug. Br J Clin Pharmacol *75*, 303–312.

McAllister, S.D., Soroceanu, L., and Desprez, P.-Y. (2015). The antitumor activity of plant-derived non-psychoactive cannabinoids. J Neuroimmune Pharmacol *10*, 255–267.

McFadden, J.W., and Corl, B.A. (2009). Activation of AMP-activated protein kinase (AMPK) inhibits fatty acid synthesis in bovine mammary epithelial cells. Biochem. Biophys. Res. Commun. *390*, 388–393.

McPartland, J.M., Duncan, M., Di Marzo, V., and Pertwee, R.G. (2015). Are cannabidiol and Δ(9) -tetrahydrocannabivarin negative modulators of the endocannabinoid system? A systematic review. Br. J. Pharmacol. *172*, 737–753.

Meyer-Arendt, K., Old, W.M., Houel, S., Renganathan, K., Eichelberger, B., Resing, K.A., and Ahn, N.G. (2011). IsoformResolver: A Peptide-Centric Algorithm for Protein Inference. Journal of Proteome Research *10*, 3060–3075.

Miller, I., Scheffer, I.E., Gunning, B., Sanchez-Carpintero, R., Gil-Nagel, A., Perry, M.S., Saneto, R.P., Checketts, D., Dunayevich, E., Knappertz, V., et al. (2020). Dose-Ranging Effect of Adjunctive Oral Cannabidiol vs Placebo on Convulsive Seizure Frequency in Dravet Syndrome: A Randomized Clinical Trial. JAMA Neurol.

Mollinedo, F., and Gajate, C. (2015). Lipid rafts as major platforms for signaling regulation in cancer. Adv Biol Regul *57*, 130–146.

Munday, M.R. (2002). Regulation of mammalian acetyl-CoA carboxylase. Biochem Soc Trans *30*, 1059–1064.

Naito, T., Ercan, B., Krshnan, L., Triebl, A., Koh, D.H.Z., Wei, F.-Y., Tomizawa, K., Torta, F.T., Wenk, M.R., and Saheki, Y. (2019). Movement of accessible plasma membrane cholesterol by the GRAMD1 lipid transfer protein complex. Elife *8*.

Nemkov, T., Hansen, K.C., and D'Alessandro, A. (2017). A three-minute method for high-throughput quantitative metabolomics and quantitative tracing experiments of central carbon and nitrogen pathways. Rapid Communications in Mass Spectrometry *31*, 663–673.

Nemkov, T., Reisz, J.A., Gehrke, S., Hansen, K.C., and D'Alessandro, A. (2019). High-throughput metabolomics: Isocratic and gradient mass spectrometry-based methods. In Methods in Molecular Biology, (Humana Press Inc.), pp. 13–26.

Norris, J.L., Farrow, M.A., Gutierrez, D.B., Palmer, L.D., Muszynski, N., Sherrod, S.D., Pino, J.C., Allen, J.L., Spraggins, J.M., Lubbock, A.L.R., et al. (2017). Integrated, High-Throughput, Multiomics Platform Enables Data-Driven Construction of Cellular Responses and Reveals Global Drug Mechanisms of Action. Journal of Proteome Research *16*, 1364–1375.

Ortegren, U., Karlsson, M., Blazic, N., Blomqvist, M., Nystrom, F.H., Gustavsson, J., Fredman, P., and Strålfors, P. (2004). Lipids and glycosphingolipids in caveolae and

surrounding plasma membrane of primary rat adipocytes. Eur. J. Biochem. *271*, 2028–2036.

Pan, H., Mukhopadhyay, P., Rajesh, M., Patel, V., Mukhopadhyay, B., Gao, B., Haskó, G., and Pacher, P. (2009). Cannabidiol attenuates cisplatin-induced nephrotoxicity by decreasing oxidative/nitrosative stress, inflammation, and cell death. J. Pharmacol. Exp. Ther. *328*, 708–714.

Pani, B., and Singh, B.B. (2009). Lipid rafts/caveolae as microdomains of calcium signaling (Elsevier Ltd).

Pirmoradi, L., Seyfizadeh, N., Ghavami, S., Zeki, A.A., and Shojaei, S. (2019). Targeting cholesterol metabolism in glioblastoma: a new therapeutic approach in cancer therapy. J. Investig. Med. *67*, 715–719.

Rajesh, M., Mukhopadhyay, P., Bátkai, S., Patel, V., Saito, K., Matsumoto, S., Kashiwaya, Y., Horváth, B., Mukhopadhyay, B., Becker, L., et al. (2010). Cannabidiol attenuates cardiac dysfunction, oxidative stress, fibrosis, and inflammatory and cell death signaling pathways in diabetic cardiomyopathy. J. Am. Coll. Cardiol. *56*, 2115–2125.

Reisz, J.A., Zheng, C., D'Alessandro, A., and Nemkov, T. (2019). Untargeted and Semi-targeted Lipid Analysis of Biological Samples Using Mass Spectrometry-Based Metabolomics. Methods Mol. Biol. *1978*, 121–135.

Rimmerman, N., Juknat, A., Kozela, E., Levy, R., Bradshaw, H.B., and Vogel, Z. (2011). The Non-Psychoactive Plant Cannabinoid, Cannabidiol Affects Cholesterol Metabolism-Related Genes in Microglial Cells. Cellular and Molecular Neurobiology *31*, 921–930.

Rimmerman, N., Ben-Hail, D., Porat, Z., Juknat, A., Kozela, E., Daniels, M.P., Connelly, P.S., Leishman, E., Bradshaw, H.B., Shoshan-Barmatz, V., et al. (2013). Direct modulation of the outer mitochondrial membrane channel, voltage-dependent anion channel 1 (VDAC1) by cannabidiol: a novel mechanism for cannabinoid-induced cell death. Cell Death & Disease *4*, e949–e949.

Ross, H.R., Napier, I., and Connor, M. (2008). Inhibition of recombinant human T-type calcium channels by Delta9-tetrahydrocannabinol and cannabidiol. J. Biol. Chem. *283*, 16124–16134.

Ryazanov, A.G., Shestakova, E.A., and Natapov, P.G. (1988). Phosphorylation of elongation factor 2 by EF-2 kinase affects rate of translation. Nature *334*, 170–173.

Ryberg, E., Larsson, N., Sjögren, S., Hjorth, S., Hermansson, N.O., Leonova, J., Elebring, T., Nilsson, K., Drmota, T., and Greasley, P.J. (2007). The orphan receptor GPR55 is a novel cannabinoid receptor. British Journal of Pharmacology *152*, 1092–1101.

Schaffer, B.E., Levin, R.S., Hertz, N.T., Maures, T.J., Schoof, M.L., Hollstein, P.E., Benayoun, B.A., Banko, M.R., Shaw, R.J., Shokat, K.M., et al. (2015). Identification of AMPK Phosphorylation Sites Reveals a Network of Proteins Involved in Cell Invasion and Facilitates Large-Scale Substrate Prediction. Cell Metabolism *22*, 907–921.

Schroeder, R., London, E., and Brown, D. (1994). Interactions between saturated acyl chains confer detergent resistance on lipids and glycosylphosphatidylinositol (GPI)-anchored proteins: GPI-anchored proteins in liposomes and cells show similar behavior. Proc. Natl. Acad. Sci. U.S.A. *91*, 12130–12134.

Serini, S., Trombino, S., Oliva, F., Piccioni, E., Monego, G., Resci, F., Boninsegna, A., Picci, N., Ranelletti, F.O., and Calviello, G. (2008). Docosahexaenoic acid induces apoptosis in lung cancer cells by increasing MKP-1 and down-regulating p-ERK1/2 and p-p38 expression. Apoptosis *13*, 1172–1183.

Serra, M., and Saba, J.D. (2010). Sphingosine 1-phosphate lyase, a key regulator of sphingosine 1-phosphate signaling and function. Adv. Enzyme Regul. *50*, 349–362.

Shaw, R.J., Kosmatka, M., Bardeesy, N., Hurley, R.L., Witters, L.A., DePinho, R.A., and Cantley, L.C. (2004). The tumor suppressor LKB1 kinase directly activates AMP-activated kinase and regulates apoptosis in response to energy stress. Proc. Natl. Acad. Sci. U.S.A. *101*, 3329–3335.

Shin, S., Jing, K., Jeong, S., Kim, N., Song, K.-S., Heo, J.-Y., Park, J.-H., Seo, K.-S., Han, J., Park, J.-I., et al. (2013). The omega-3 polyunsaturated fatty acid DHA induces simultaneous apoptosis and autophagy via mitochondrial ROS-mediated Akt-mTOR signaling in prostate cancer cells expressing mutant p53. Biomed Res Int *2013*, 568671.

Silvestri, C., Paris, D., Martella, A., Melck, D., Guadagnino, I., Cawthorne, M., Motta, A., and Di Marzo, V. (2015). Two non-psychoactive cannabinoids reduce intracellular lipid levels and inhibit hepatosteatosis. Journal of Hepatology *62*, 1382–1390.

Silvius, J.R. (2003). Role of cholesterol in lipid raft formation: lessons from lipid model systems. Biochim. Biophys. Acta *1610*, 174–183.

Smart, E.J., Ying, Y.S., Conrad, P.A., and Anderson, R.G. (1994). Caveolin moves from caveolae to the Golgi apparatus in response to cholesterol oxidation. J. Cell Biol. *127*, 1185–1197.

Sokolov, A., and Radhakrishnan, A. (2010). Accessibility of Cholesterol in Endoplasmic Reticulum Membranes and Activation of SREBP-2 Switch Abruptly at a Common Cholesterol Threshold. J. Biol. Chem. *285*, 29480–29490.

Staneva, G., Puff, N., Stanimirov, S., Tochev, T., Angelova, M.I., and Seigneuret, M. (2018). The Alzheimer's disease amyloid-β peptide affects the size-dynamics of raft-mimicking Lo domains in GM1-containing lipid bilayers. Soft Matter *14*, 9609–9618.

Sun, S.-N., Jia, W.-D., Chen, H., Ma, J.-L., Ge, Y.-S., Yu, J.-H., and Li, J.-S. (2013). Docosahexaenoic acid (DHA) induces apoptosis in human hepatocellular carcinoma cells. Int J Clin Exp Pathol *6*, 281–289.

Supek, F., Bošnjak, M., Škunca, N., and Šmuc, T. (2011). REVIGO Summarizes and Visualizes Long Lists of Gene Ontology Terms. PLOS ONE *6*, e21800.

Thiele, E.A., Marsh, E.D., French, J.A., Mazurkiewicz-Beldzinska, M., Benbadis, S.R., Joshi, C., Lyons, P.D., Taylor, A., Roberts, C., Sommerville, K., et al. (2018). Cannabidiol in patients with seizures associated with Lennox-Gastaut syndrome (GWPCARE4): a randomised, double-blind, placebo-controlled phase 3 trial. Lancet *391*, 1085–1096.

Trapnell, C., Williams, B.A., Pertea, G., Mortazavi, A., Kwan, G., van Baren, M.J., Salzberg, S.L., Wold, B.J., and Pachter, L. (2010). Transcript assembly and quantification by RNA-Seq reveals unannotated transcripts and isoform switching during cell differentiation. Nature Biotechnology *28*, 511–515.

Venugopal, R., and Jaiswal, A.K. (1998). Nrf2 and Nrf1 in association with Jun proteins regulate antioxidant response element-mediated expression and coordinated induction of genes encoding detoxifying enzymes. Oncogene *17*, 3145–3156.

Wang, G.L., and Semenza, G.L. (1993). General involvement of hypoxia-inducible factor 1 in transcriptional response to hypoxia. Proc. Natl. Acad. Sci. U.S.A. *90*, 4304–4308.

Wang, Y., Mukhopadhyay, P., Cao, Z., Wang, H., Feng, D., Haskó, G., Mechoulam, R., Gao, B., and Pacher, P. (2017). Cannabidiol attenuates alcohol-induced liver steatosis, metabolic dysregulation, inflammation and neutrophil-mediated injury. Scientific Reports *7*, 12064.

Wassall, S.R., Leng, X., Canner, S.W., Pennington, E.R., Kinnun, J.J., Cavazos, A.T., Dadoo, S., Johnson, D., Heberle, F.A., Katsaras, J., et al. (2018). Docosahexaenoic acid regulates the formation of lipid rafts: A unified view from experiment and simulation. Biochim Biophys Acta Biomembr *1860*, 1985–1993.

Watkins, A.R. (2019). Cannabinoid interactions with ion channels and receptors. Channels (Austin) *13*, 162–167.

Whyte, L.S., Ryberg, E., Sims, N.A., Ridge, S.A., Mackie, K., Greasley, P.J., Ross, R.A., and Rogers, M.J. (2009). The putative cannabinoid receptor GPR55 affects osteoclast function in vitro and bone mass in vivo. Proc Natl Acad Sci U S A *106*, 16511–16516.

Widenmaier, S.B., Snyder, N.A., Nguyen, T.B., Arduini, A., Lee, G.Y., Arruda, A.P., Saksi, J., Bartelt, A., and Hotamisligil, G.S. (2017). NRF1 Is an ER Membrane Sensor that Is Central to Cholesterol Homeostasis. Cell *171*, 1094.e15–1109.e15.

Wiśniewski, J.R. (2016). Quantitative Evaluation of Filter Aided Sample Preparation (FASP) and Multienzyme Digestion FASP Protocols. Anal. Chem. *88*, 5438–5443.

Woods, A., Dickerson, K., Heath, R., Hong, S.-P., Momcilovic, M., Johnstone, S.R., Carlson, M., and Carling, D. (2005). Ca2+/calmodulin-dependent protein kinase kinase-beta acts upstream of AMP-activated protein kinase in mammalian cells. Cell Metab. *2*, 21–33.

Wu, H.-Y., Goble, K., Mecha, M., Wang, C.-C., Huang, C.-H., Guaza, C., and Jan, T.-R. (2012). Cannabidiol-induced apoptosis in murine microglial cells through lipid raft. Glia *60*, 1182–1190.

Zhao, Y.-F., Wang, L., Lee, S., Sun, Q., Tuo, Y., Wang, Y., Pei, J., and Chen, C. (2010). Cholesterol induces mitochondrial dysfunction and apoptosis in mouse pancreatic beta-cell line MIN6 cells. Endocr *37*, 76–82.